Fall 2021

Preclassic cultural eutrophication of lake Petén Itzá, lowland Guatemala, by the early Maya of Nixtun-Ch'ich'

Brooke A. Birkett

PRECLASSIC CULTURAL EUTROPHICATION OF LAKE PETÉN ITZÁ,

LOWLAND GUATEMALA, BY THE EARLY MAYA OF NIXTUN-CH'ICH'

by

BROOKE AMBER BIRKETT

A THESIS

Presented to the Graduate Faculty of the

MISSOURI UNIVERSITY OF SCIENCE AND TECHNOLOGY

In Partial Fulfillment of the Requirements for the Degree

MASTER OF SCIENCE

in

GEOLOGY AND GEOPHYSICS

2021

Approved by:

Jonathan Obrist-Farner, Advisor
David M. Borrok
David J. Wronkiewicz

PUBLICATION THESIS OPTION

This thesis consists of the following article, formatted in the style used by the Missouri University of Science and Technology:

Paper I, found on pages 4–73, is intended for submission to *Proceedings of the National Academy of Sciences of the United States of America*.

ABSTRACT

Paleolimnological evidence indicates the ancient Maya transformed lowland terrestrial ecosystems by felling forest vegetation to construct large civic-ceremonial centers and expand agriculture. The effects of prehistoric Maya land alterations on lake trophic status, however, remain poorly understood. We analyzed a 515-cm-long sediment core from Lake Petén Itzá, lowland Guatemala, to infer paleoenvironmental changes resulting from Maya occupation of the riparian archaeological site of Nixtun-Ch'ich'. Substantial increases in charcoal and fecal stanol concentrations indicate Maya occupation of the Candelaria Peninsula by the late Early Preclassic period beginning ca. 1400 cal yr Before the Common Era (hereafter BCE), despite scant archaeological evidence for settlement at that time. Variations in organic matter geochemical proxies reveal a period of cultural eutrophication in the western arm of the lake between ca. 760 and 20 BCE, during initial construction and later expansion of the city's unique urban grid. Deforestation, soil erosion, urbanization, and human waste efflux enhanced nutrient delivery to the lake, leading to greater primary productivity. During an ~80-year interval, from ca. 20 BCE to 60 CE, there was a decline in lake trophic state, possibly related to partial abandonment of the city in the Terminal Preclassic. Thereafter, shifts in fecal stanol concentrations throughout the Classic and Postclassic periods suggest relatively low, albeit fluctuating, human population densities. Whereas previous studies of long sediment cores from Petén waterbodies have indicated that ancient land clearance led to massive siltation, and perhaps depression of lacustrine primary production, the core collected near Nixtun-Ch'ich' shows evidence of ancient Maya cultural eutrophication.

ACKNOWLEDGMENTS

Numerous people and organizations have greatly contributed to the completion of this thesis and the included paper. We thank Evelyn Chan for arranging the construction of the coring platform in Petén and the Guatemalan Instituto de Antropología e Historia (IDEAH) for permission to export the cores. We also thank Defensores de la Naturaleza and the Consejo Nacional de Áreas Protegidas (CONAP) for providing personnel to help with coring. We also thank Edward Duarte for assistance with age-depth modeling and charcoal analysis, Patrick Cho for assistance with *n*-alkane analyses, Thi Hao Bui and Benjamin Keenan for assistance with fecal stanol and sterol analyses, and Anna Hoffmann for general laboratory assistance. We also thank Mark Brenner for insightful discussions and for his thoughtful review of the manuscript, and we thank Jeremy Maurer for insightful discussions.

This work was partially supported by NSF/GSA (National Science Foundation/Geological Society of America) Graduate Student Geoscience Grant # 13171-21, which was funded by NSF Award # 1949901. This research was also partially supported by Society for Sedimentary Geology (SEPM) Student Research Grants and the Dr. Alfred Spreng Graduate Research Award (Missouri University of Science and Technology).

TABLE OF CONTENTS

LIST OF ILLUSTRATIONS

PAPER Page

NOMENCLATURE

Symbol	Description
$\delta^{13}C_{org}$	Carbon Stable Isotopes of Bulk Organic Matter
$\delta^{15}N_{org}$	Nitrogen Stable Isotopes of Bulk Organic Matter
cal yr	calibrated years
ca.	circa
copro	coprostanol
epicopro	epicoprostanol
BCE	Before the Common Era
CE	Common Era
OC	Organic Carbon
OM	Organic Matter
TC	Total Carbon
TIC	Total Inorganic Carbon
TN	Total Nitrogen
TOC	Total Organic Carbon
wt%	weight %

1. INTRODUCTION

1.1. OVERVIEW

Ancient Maya civilization persisted for thousands of years, with early largescale settlement beginning in the Middle Preclassic Period (ca. 900/800 BCE) across eastern Mexico, Guatemala, and Belize. Several early Maya sites persisted throughout and after the Late Preclassic Period, although some experienced a Terminal Preclassic decline ca. 100–250 CE (Dunning et al., 2012). Maya civilization flourished during the Classic Period, with the construction of large civic-ceremonial centers, such as Tikal and Chich'en Itzá. However, there was widespread socio-political collapse and depopulation ca. 950–1000 CE at the end of the Classic Period (Turner II and Sabloff, 2012), potentially associated with climatic drying (Hodell et al., 1995; Dunning et al., 2012; Douglas et al., 2015; Douglas et al., 2016), soil degradation, disease, and warfare (Adams, 1973).

Maya land alterations associated with natural resource extraction (e.g., mining of limestone bedrock or felling of forests for lumber), agriculture, or urbanization ca. 1000 BCE–1000 CE have been used to describe an "Early Anthropocene", or "Mayacene" (Beach et al., 2015; Beach et al., 2019; Krause et al., 2021). Extensive land alterations commonly resulted in increased soil erosion, causing siltation of waterbodies and deposition of thick units of inorganic colluvium during the Preclassic and Classic periods (ca. 900 BCE–950 CE) known as the "Maya clay" (Deevey et al., 1979; Anselmetti et al., 2007; Mueller et al., 2009; Wahl et al., 2013; Battistel et al., 2018). Previous studies suggest that intense siltation of waterbodies, as a result of ancient Maya land alterations, suppressed lacustrine primary production by limiting light penetration and adsorbing dissolved nutrients (Deevey, 1985; Brenner et al., 2002). However, it is difficult to envision that the establishment of large urban centers along the shorelines of Petén waterbodies by the Maya, which would have increased nutrient loading to the lakes, did not have a major impact on trophic status.

Today, cultural eutrophication is a common environmental issue affecting lakes worldwide, from urban areas in China (e.g., Li et al., 2019) to sparsely populated expanses in the high arctic (e.g., Gallant et al., 2020). The recognition of cultural eutrophication as a modern water quality concern has sparked research on lake response to engineered treatments (e.g., Chorus et al., 2020; Jilbert et al., 2020; Singh and Patidar, 2020), but these studies are temporally limited. Examination of a historical analog for cultural eutrophication can provide insight into the timing, extent, and nature of lake system recovery over decadal to centennial timescales after the reduction or cessation of prolonged anthropogenic disturbances.

1.2. STUDY AREA

The central Petén lakes region of northern Guatemala consists of eight lakes that formed in karst depressions along an east-west normal fault (Vinson, 1962). Several Maya archaeological sites are situated along the shorelines of these lakes. Lake Petén Itzá is the largest of these waterbodies and contains two sub-basins (north and south) that are separated by two peninsulas (Tayasal and Candelaria). The riparian archaeological site of Nixtun-Ch'ich', the focus of this study, lies on the Candelaria Peninsula on the western side of the lake. This civic-ceremonial site contains a unique urban grid with paved corridors and canals that functioned together as a drainage system for the city (Pugh et al., in press). Additionally, Nixtun-Ch'ich' was an ideological focal point of Preclassic Maya civilization, and archaeological studies have identified six satellites of the city with similar ritual architectural complexes oriented to solar phenomena (Rice and Pugh, 2021).

1.3. PURPOSE

This study provides a unique example that uses history as an experimental laboratory to examine the effects of anthropogenic activities on lacustrine environments over decadal to centennial time scales. Here, we examine a 515-cm-long sediment core from the western arm of Lake Petén Itzá, northern Guatemala, collected adjacent to the ancient Maya archaeological site of Nixtun-Ch'ich'. The primary purpose of this investigation is to characterize lake and catchment conditions prior to significant Maya settlement and disturbance and interpret how conditions changed as a result of Maya activities in Nixtun-Ch'ich'. Furthermore, we interpret lake response to the abrupt reduction or cessation of anthropogenic disturbances and compare pre- and post-disturbance conditions. The second objective of this study is to build upon the findings of archaeological investigations and improve the record of the settlement history of Nixtun-Ch'ich' using fecal sterol and stanol analyses.

PAPER

I. PRECLASSIC CULTURAL EUTROPHICATION OF LAKE PETÉN ITZÁ, GUATEMALA, BY THE EARLY MAYA OF NIXTUN-CH'ICH'

Brooke A. Birkett[1], Jonathan Obrist-Farner[1], Prudence M. Rice[2], Wesley G. Parker[3], Peter M.J. Douglas[3], Melissa A. Berke[4], Audrey K. Taylor[4], Jason H. Curtis[5]

[1]Geosciences and Geological and Petroleum Engineering Department, Missouri University of Science and Technology, Rolla, Missouri, USA 65409

[2]Department of Anthropology (emerita), Southern Illinois University Carbondale, Carbondale, Illinois, USA 62901

[3]Department of Earth and Planetary Sciences, McGill University, Montreal, Quebec, Canada H3A 0E8

[4]Civil and Environmental Engineering and Earth Sciences Department, University of Notre Dame, Notre Dame, Indiana, USA 46556

[5]Department of Geological Sciences, University of Florida, Gainesville, Florida, USA 32611

ABSTRACT

Paleolimnological evidence indicates the ancient Maya transformed lowland terrestrial ecosystems by felling forest vegetation to construct large civic-ceremonial centers and expand agriculture. The effects of prehistoric Maya land alterations on lake trophic status, however, remain poorly understood. We analyzed a 515-cm-long sediment core from Lake Petén Itzá, lowland Guatemala, to infer paleoenvironmental changes resulting from Maya occupation of the riparian archaeological site of Nixtun-Ch'ich'. Substantial increases in charcoal and fecal stanol concentrations indicate Maya occupation of the Candelaria Peninsula by the late Early Preclassic period beginning ca. 1400 cal yr BCE (hereafter BCE), despite scant archaeological evidence for settlement at that time. Variations in organic matter geochemical proxies reveal a period of cultural eutrophication in the western arm of the lake between ca. 760 and 20 BCE, during initial construction and later expansion of the city's unique urban grid. Deforestation, soil erosion, urbanization, and human waste efflux enhanced nutrient delivery to the lake, leading to greater primary productivity. During an ~80-year interval, from ca. 20 BCE to 60 CE, there was a decline in lake trophic state, possibly related to partial abandonment of the city in the Terminal Preclassic. Thereafter, shifts in fecal stanol concentrations throughout the Classic and Postclassic periods suggest relatively low, albeit fluctuating, human population densities. Whereas previous studies of long sediment cores from Petén waterbodies have indicated that ancient land clearance led to massive siltation, and perhaps depression of lacustrine primary production, the core collected near Nixtun-Ch'ich' shows evidence of ancient Maya cultural eutrophication.

1. INTRODUCTION

Paleolimnological studies have documented the impacts of ancient Maya activities on the lowland terrestrial environments of eastern Mexico, Guatemala, and Belize, specifically through widespread deforestation for urbanization and agricultural development (Deevey et al., 1979; Islebe et al., 1996; Curtis et al., 1998; Leyden et al., 1998; Rosenmeier et al., 2002; Wahl et al., 2013; Battistel et al., 2018; Obrist-Farner and Rice, 2019). Land clearance in the hilly terrain of the region led to rapid soil erosion and siltation of waterbodies, recorded as thick deposits of inorganic colluvium sometimes referred to as "Maya clay" that accumulated during the Preclassic (ca. 900 BCE–200 CE) and Classic (200–950 CE) Maya archaeological periods (Deevey et al., 1979; Anselmetti et al., 2007; Mueller et al., 2009; Wahl et al., 2013; Battistel et al., 2018). Ancient Maya occupation was also linked to periods of high fire frequency, likely related to the early use of slash-and-burn (swidden) agricultural techniques (Schüpbach et al., 2015). The prominence of large-scale ancient Maya land alterations during the Preclassic and Classic periods has also been used to suggest an "Early Anthropocene", or "Mayacene", ca. 1000 BCE–1000 CE (Beach et al., 2015; Beach et al., 2019; Krause et al., 2021). However, these studies primarily focus on evidence for vast human-mediated land transformations rather than lacustrine ecosystem responses to anthropogenic disturbances during those times.

Widespread land-cover change might be expected to have influenced the trophic status of local lakes, through enhancement of nutrient loading and consequent shifts in aquatic community composition. Despite the presence of archaeologically documented, dense Maya populations around the lakes in central Petén, northern Guatemala, paleolimnological studies have so far failed to reveal evidence of cultural eutrophication as a result of Maya activities. It has been suggested that intense siltation limited light penetration and adsorbed dissolved nutrients, thereby suppressing primary production (Deevey, 1985; Brenner et al., 2002). However, given evidence for recent trophic state increase in Lake Petén Itzá, Guatemala associated with rapid population growth in the 20th century (Rosenmeier et al., 2004; Pérez et al., 2010), it seems likely that the establishment of ancient Maya urban centers near the waterbodies would have also influenced lake trophic status.

Here, we conduct a multi-proxy paleolimnological investigation on a radiocarbon-dated sediment core from Lake Petén Itzá, lowland Guatemala. The core was collected from the western arm of the lake, adjacent to a southern lowland Maya archaeological site on the Candelaria Peninsula called Nixtun-Ch'ich' (Figure 1). Stratigraphic fluctuations in several organic matter geochemical proxies reveal a previously undocumented period of cultural eutrophication during times of Maya occupation at Nixtun-Ch'ich' from ca. 760 to 20 BCE, providing further evidence of anthropogenic environmental impacts in the Early Anthropocene. The onset of eutrophic conditions coincides with dense early Maya occupation at the site and changes in land-use practices, suggesting that prolonged and spatially concentrated ancient human activities had a profound impact on this shallow arm of the lake. Whereas massive Maya-induced siltation in other Petén lakes may have suppressed lake productivity, paving of the riparian gridded city of Nixtun-Ch'ich' may have enhanced nutrient-laden runoff from the urban center, which fueled primary productivity in the relatively shallow and hydrologically isolated western basin of Lake Petén Itzá. A sharp decrease in lithogenic elements (e.g., titanium) at the top of the disturbance zone in the core (ca. 20 BCE; 95% range 334 BCE–298 CE) indicates abrupt reduction or cessation of human constructional activities toward the end of the Late Preclassic (ca. 400 BCE–100 CE), and the lake experienced a relatively swift, but incomplete, recovery within less than approximately 80 years. The sediment record from Lake Petén Itzá enabled us to investigate the causes and timing of cultural eutrophication during ancient Maya occupation, and explore the lake response to changing human-mediated catchment conditions over decadal to centennial time scales.

2. SIGNIFICANCE STATEMENT

Previous paleolimnological studies of Petén lakes, northern Guatemala, failed to detect evidence of cultural eutrophication as a result of ancient Maya settlement, despite archaeological evidence for dense human populations around the waterbodies. This study alters the narrative on the environmental impacts of lowland Maya civilization, providing new insights into the consequences of construction and occupation of the city of Nixtun-Ch'ich', where dense Middle and Late Preclassic Maya settlement led to enhanced soil erosion and nutrient delivery to the western arm of Lake Petén Itzá. This study documents how lake trophic state increased as a consequence of protracted riparian human activities, and how the lake responded to the termination of early construction and probable partial abandonment in the Terminal Preclassic.

3. STUDY SITE

Lake Petén Itzá is the largest (~100 km^2) and deepest (165 m) of eight large, closed-basin waterbodies in the central Petén lakes region of northern Guatemala (Figure 1). The lake occupies two connected basins that formed in karst depressions in marine limestones of Late Cretaceous to Tertiary and Paleocene-Eocene-age (Vinson, 1962; Hodell et al., 2004). The lake's larger, deeper northern basin is bounded on the north shore by the steep wall of an east-west normal fault (Vinson, 1962; Anselmetti et al., 2006), and the southern basin has a gently sloping bathymetry, with water depths of less than 20 meters (Brenner, 2018).

The 515-cm-long sediment core (PI-NC-1) was collected in July 2018, in 8.4 meters of water ~200 m south (16°56’36” N, 89°55’56” W) of the early Maya archaeological site of Nixtun-Ch’ich’, in the narrow, western arm (7 km long x 250–450

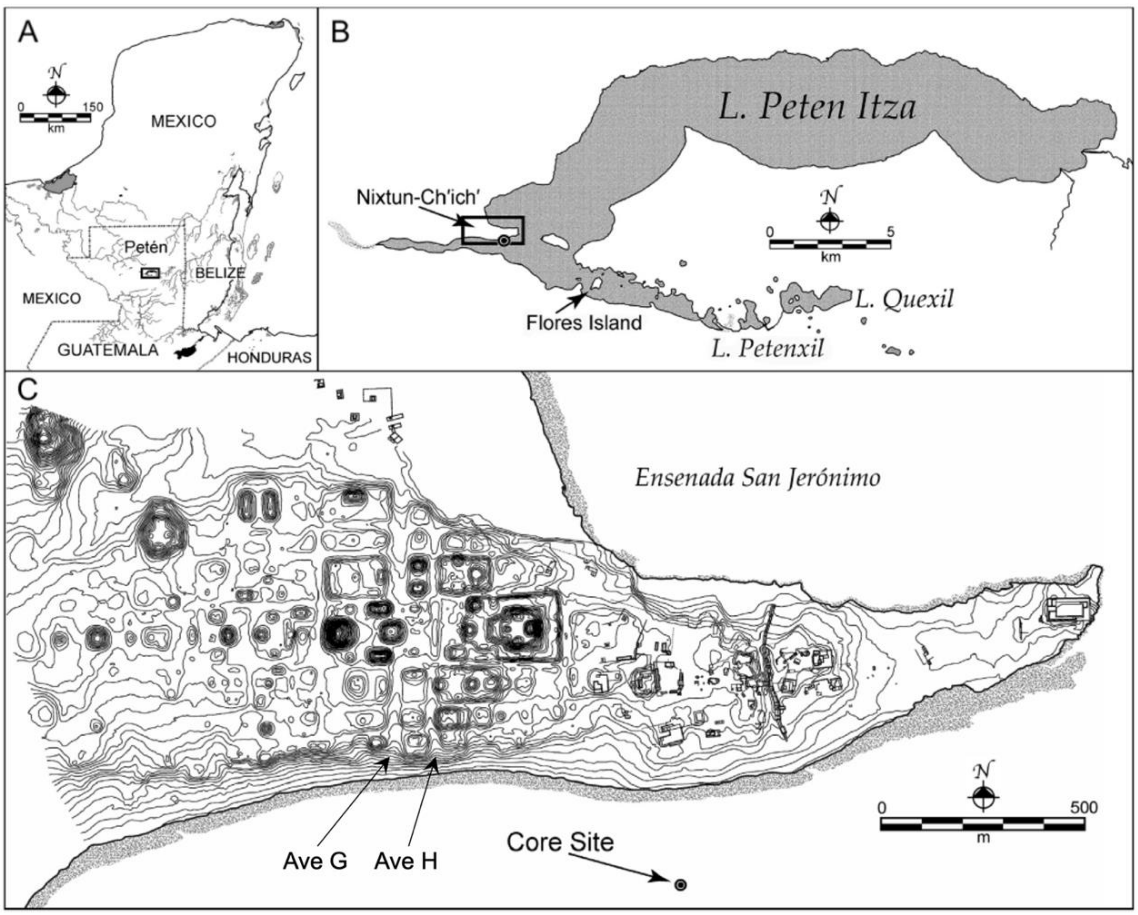

Figure 1. Location map. A) Map showing the Maya lowlands on the Yucatán Peninsula, with the location of Lake Petén Itzá indicated by the small rectangle in northern Guatemala. B) Outline map of Lake Petén Itzá, showing the location of the archaeological site of Nixtun-Ch’ich’ at the western end of the lake. C) Map of the Candelaria Peninsula showing the unique gridded layout of Nixtun-Ch’ich’ and the locations of Avenues G and H, as well as the site where the lake sediment core was collected (modified from Obrist-Farner and Rice, 2019).

m wide) of the lake's southern basin (Figure 1). Nixtun-Ch'ich' contains an urban core that covers 1.1 km^2 and is centered by an *axis urbis* (Rice and Pugh, 2021). The city also features a unique, modular, urban gridded layout consisting of seven north-south "avenues" that intersect with six east-west "streets", covering an area of 2.5 km^2 (Pugh and Rice, 2017; Pugh, 2019). This system of roughly orthogonal corridors, which was supplemented with canals in areas that likely experienced intense flow during rainfall events, facilitated drainage from the site (Pugh et al., in press). The core site lies downstream and bathymetrically downgradient from two of the archaeological site's major north-south trending avenues (G and H), which run adjacent to major structures in Nixtun-Ch'ich' and likely served as focal points for the delivery of dissolved and suspended material in runoff to this arm of the lake (Figure 1).

Nixtun-Ch'ich' was a long-lived civic-ceremonial center that was first occupied in the late or terminal Early Preclassic period (pre-900/800 BCE), as determined from scattered, small pottery fragments (Rice, 2019). Stratified occupation and construction began in the Middle Preclassic period (ca. 900/800–500/400 BCE) and was sustained through the Late Preclassic. Archaeological excavations date initial emplacement of the site's atypical urban gridded structure to the heavily occupied Middle Preclassic period (ca. 800–500 BCE; Pugh and Rice, 2017; Pugh, 2019). Substantial construction of the city continued into the Late Preclassic period (Rice, 2019) and ended around 100 CE. Cessation of building and/or partial abandonment of the site (Obrist-Farner and Rice, 2019) coincides with a proposed "Late Preclassic Collapse" that has been identified at other southern Maya lowland centers (Dunning et al., 2012). Afterwards, occupation of the site persisted through the Classic and Postclassic periods, and beyond the Spanish conquest (1697 CE; Jones, 1998) into Colonial times (Rice, 2009; Rice, 2019).

4. MATERIALS AND METHODS

4.1. OVERVIEW

In July 2018, we collected two sediment cores from Lake Petén Itzá, in the vicinity of the southern lowland Maya site of Nixtun-Ch'ich'. Here, we report the findings from one of the cores (PI-NC-1) and expand upon the findings by Obrist-Farner and Rice (2019).

4.2. CORE COLLECTION

The 515-cm-long sediment core (PI-NC-1) was collected ~200 m south of the Maya archaeological site of Nixtun-Ch'ich' (16°56'36" N, 89°55'56" W), in the narrow, western arm (7 km long and 250–450 m wide) of the southern basin of the lake (Figure 1). The location is downgradient from Avenues G and H in the city (Figure 1), which run adjacent to major structures in Nixtun-Ch'ich' and carried runoff from the site into the lake. The core was collected in 8.4 m of water from a wooden platform mounted on two *lanchas* (motorized canoes). The 72-cm mud-water interface (MWI) core was collected using a modified piston corer designed to obtain undisturbed MWI sediments (Fisher et al., 1992). The unconsolidated MWI sediments were extruded vertically in the field, sectioned at 2.0-cm intervals, and placed into labeled Whirl-Pak™ bags. Next, six sequential sections of core were collected from 50 to 515 cm depth using a modified

Livingstone-type piston corer designed for collection of deeper, consolidated deposits. These core sections were kept in labeled polycarbonate tubes that were wrapped in plastic. After collection, core material was transported to the laboratory for further analysis. The core was divided into four stratigraphic zones based on physical properties of the sediment (color, texture, grain size). Here, we present findings from the first three zones.

4.3. AGE-DEPTH MODELING

We refined the existing age-depth model for the PI-NC-1 core that was presented in Obrist-Farner and Rice (2019) and used six radiocarbon dates. This study used an additional sample of terrestrial wood charcoal from a depth of 218 cm (Table S1 in Supplementary Information). The sample was washed with deionized water over a 125-μm sieve to remove adhering sediment, wrapped in aluminum foil, and submitted to the Center for Accelerator Mass Spectrometry at Lawrence Livermore National Laboratory. We created a new age-depth model (Figure S1 in Supplementary Information) by applying the Bayesian software Bacon (rbacon package in R; Blaauw and Christen, 2011) to the seven radiocarbon dates, calibrated with IntCal20 (Reimer et al., 2020), and the date the core was collected (2018). All dates came from terrestrial wood (charcoal) to avoid potential effects from “hard-water-lake error,” which may confound dates on bulk organic matter in this limestone bedrock region (Curtis et al., 1998; Islebe et al., 1996). We report weighted mean date estimates from the age-depth model to characterize the timing of changes detected in the core.

4.4. GEOCHEMICAL ANALYSIS

Samples for geochemical analyses were collected at 5-cm intervals along the length of the core, from 313 to 53 cm depth. Samples from the uppermost 50 cm, from the MWI core, were collected at intervals of 4 or 6 cm. Samples were oven-dried at 60°C for 15 h, ground to a fine powder with a ceramic mortar and pestle, and placed into labeled 20-mL scintillation vials. Total carbon (TC) and total nitrogen (TN) were measured using a Carlo Erba NA 1500 CNS elemental analyzer. Total inorganic carbon (TIC) was determined by coulometric titration using an AutoMate^{TM} acidification preparation device coupled with a UIC^{TM} 5017 CO_2 coulometer. Total organic carbon (TOC) was calculated as TC minus TIC. TOC/TN mass ratios (i.e., C/N ratios) were computed by dividing TOC (wt %) by TN (wt %). Samples for bulk carbon stable isotope ($\delta^{13}C_{org}$) analysis were treated with 1 N HCl to remove carbonate and then washed with distilled water to remove chloride. Samples for nitrogen stable isotope ($\delta^{15}N_{org}$) analysis of bulk organic matter were not acidified. Samples were loaded into tin capsules and placed in a 50-position automated carousel on a Carlo Erba NA 1500 elemental analyzer. After combustion at 1020°C, gases were carried in a helium stream through a Conflo II interface to a Thermo Electron DeltaV Advantage isotope ratio mass spectrometer to measure the carbon and nitrogen stable isotope compositions of bulk organic matter. Carbon isotope results are expressed as per mil (‰) in standard delta notation relative to Vienna Pee Dee Belemnite (VPDB). Nitrogen isotope results are expressed as the per mil (‰) deviation from atmospheric nitrogen (AIR, $\delta^{15}N_{org} = 0$). We also calculated the mean and 2 standard deviation (2σ) ranges of C/N mass ratios and $\delta^{13}C_{org}$ for each zone (Figure

4; Figure S4 and Table S2 in Supplementary Information) to determine whether the values reflect statistically similar or different lake conditions in each zone.

4.5. *n*-ALKANE QUANTIFICATION

For *n*-alkane quantification, 38 samples were collected across 2-cm intervals from 13 cm to 310 cm core depth. Freeze-dried and homogenized samples (2.05–8.95 g) were extracted using an accelerated solvent extractor (ASE) with 9:1 (*v:v*) dichloromethane:methanol (DCM:MeOH). The total lipid extract (TLE) was then separated using a deactivated alumina oxide column to isolate the apolar fraction containing the *n*-alkanes using 9:1 hexane:DCM solution and purified using Ag^+ impregnated silica gel column chromatography and hexane eluant to isolate the saturated hydrocarbons. Samples were spiked with 50 ng/µL 5α-Androstane standard and analyzed using a Thermo Trace Ultra ISQ gas chromatograph (GC) with a mass spectrometer (MS) and a flame ionization detector (FID) to identify and quantify the *n*-alkanes, respectively. Samples were injected at 300°C with a 30-m fused silica column (DB-5, 0.25 mm ID, 0.25 µm film thickness) using hydrogen as the carrier gas. Following a 1-minute hold at 80°C, the GC oven temperature was ramped to 320°C at a rate of 13°C/min, with a final hold of 20 minutes. The *n*-alkanes were identified by retention times of a standard *n*-alkane mix and through comparison of fragmentation patterns in an MS library. Quantification of *n*-alkanes was ascertained via comparison of GC-FID sample peak integration to the standard, and the total *n*-alkane abundance is expressed as the summed absolute concentration of C_{16} to C_{35} relative to dry sediment weight (µg/g dry sediment).

4.6. FECAL STEROID ANALYSIS

For fecal stanol/sterol quantification, 59 samples were collected along the length of the 515-cm core. Samples were freeze-dried, homogenized, and weighed. Then, sediment samples were placed in PTFE tubes and extracted using a CEM MARS 6 microwave extractor heated at 80°C for 20 minutes with 10 mL of 9:1 DCM:MeOH solution. The contents of the PTFE tubes were then transferred to centrifuge vials and centrifuged to obtain the TLE. Next, each TLE was run through a chromatographic column containing 5 cm of sodium sulphate to isolate the non-polar fraction with 15 mL of hexane and the neutral and polar fractions with 15 mL of methanol. The solution containing the neutral and polar fractions was saponified using KOH and separated into sterol and fatty acid fractions using liquid-liquid extractions with 10 mL of 2:1 hexane:dichloromethane solution. The sterol fraction was then fully evaporated and derivatized with 200 µL each of BSTFA (bis-trimethyl silyl trifluoroacetamide) and pyridine to replace the hydrogen with the less exchangeable trimethylsilyl (TMS) group. The neutral (sterol) fraction was analyzed using gas chromatography with a flame ionization detector (GC-FID) with a TRACE TR-5 GC Column (60 m x 0.25 mm) in sequence with known standards for cholestanol, cholesterol, stigmastanol, coprostanol, and epicoprostanol (Sigma-Aldrich) in order to quantify the compounds as compared to the standards via peak integration. Fecal steroid concentrations include all isomers of the compounds and are expressed as absolute concentrations relative to dry sediment weight (µg/g dry sediment) and normalized to TOC (µg/g of OC). For interpretation of stanol/sterol abundances, we focus on concentrations normalized to TOC to account for the effects of mineral dilution, as well as the potential effects of organic matter deposition and preservation on stanol/sterol concentrations (LeBlanc et al., 1992; Thienemann et al., 2017). We report the sum of epicoprostanol and coprostanol (after White et al., 2018 and Keenan et al., 2021) because it was not possible to consistently resolve these molecules due to their similar retention times. Epicoprostanol is a transformation product of coprostanol in the environment (Bull et al., 2002), so their summed concentration represents the net input of coprostanol to lake sediments.

4.7. CHARCOAL ANALYSIS

Charcoal analyses were carried out following the macroscopic sieve procedure of the National Lacustrine Core Facility (LacCore) at University of Minnesota, outlined below. For the analyses, ~1 cm^3 of wet sample was collected from 2-cm core depth intervals in MWI sediments and 1-cm core depth intervals from depths of 50 to 313 cm. Samples were first treated with ~25 mL hydrogen peroxide (6%), covered with aluminum foil, and heated at ~50°C for 24 h to oxidize organic matter. Next, each sample was washed gently over a 125-μm sieve, and the retained fraction was collected into a 100 mm x 15 mm polystyrene petri dish. Charcoal particles >125 μm are likely to have been derived from local, rather than distant, fires, thus representing the fire history in the immediate vicinity of the core location (Whitlock and Larsen, 2001). Next, approximately 15 mL hydrogen peroxide (6%) was added to the petri dish and the sample was covered with aluminum foil and allowed to dry for 24–72 h at ~50°C. After drying, macroscopic charcoal particles were counted under a Leica S9i microscope at 25x magnification.

5. RESULTS AND INTERPRETATION

5.1. OVERVIEW

We modified the age-depth model of sediment core PI-NC-1 used in Obrist-Farner and Rice (2019) by including an additional radiocarbon date (Figure S1 and Table S1 in Supplementary Information). Dates on samples of terrestrial wood charcoal were all in stratigraphic order, and the 515-cm core captures the last ~7,000 years. We subdivided the core into four sediment zones based on physical characteristics of the sediment (color, texture, grain size). Here, we present data from 313 to 58 cm core depth from the first three zones of the core, spanning the interval from ca. 2065 BCE to 1510 CE. First, we present data from the upper portion of Zone 1, spanning from ca. 2065 to 760 BCE, which consists of gray, thickly laminated to very thinly bedded, carbonate-rich silty clays with variable amounts of gastropod shells (Figs. 2 & 3). Then, we specifically focus on the interval between 209 cm (763 BCE; 95% range 916–579 BCE) and 164 cm (18 BCE; 95% range 334 BCE–298 CE), which exhibits distinctive sediment characteristics. This interval of sediment (Zone 2) changes to a dark brown-gray, massive, carbonate-rich clay with very sparse organic debris and gastropod shell fragments (Figs. 2 & 3). Zone 2 is coeval with the "Maya clay" unit observed in sediment cores from several lakes across the southern Maya lowlands (Deevey et al., 1979; Anselmetti et al., 2007; Wahl et al., 2013). Zone 3 spans from ca. 20 BCE to 1510 CE and consists of light brown, very thinly bedded, organic and carbonate-rich silty clays with variable amounts of gastropod shell fragments (Figs. 2 & 3).

5.2. ZONE 1 (2065–760 BCE)

Geochemical data in Zone 1 exhibit relatively constant values from about 2065 to 760 BCE, representing relatively stable, pre-disturbance lake conditions prior to substantial anthropogenic activity near the core location. Total organic carbon (TOC) and total nitrogen (TN) remained relatively constant, with average values of 2.8 ± 0.6 and 0.2 ± 0.03 wt%, respectively (Figure 3). TOC/TN mass ratios (i.e., C/N ratios) were also relatively constant and averaged 13.5 ± 1.1 (Figure 2), suggesting mixed input of organic matter (OM) from both lacustrine algae and terrestrial and aquatic plants (Meyers and Teranes, 2001; Fellerhoff et al., 2003). Nitrogen and carbon stable isotope values of bulk organic matter ($\delta^{15}N_{org}$ and $\delta^{13}C_{org}$) had average values of 2.7 ± 0.4‰ and -25.0 ± 0.7‰, respectively (Figure 2). The mean carbon stable isotope value indicates that sediment OM was derived primarily from lake algae and C_3 land and aquatic plants (Meyers and Teranes, 2001; Fellerhoff et al., 2003). The total *n*-alkane (saturated hydrocarbon) abundance, which reflects a fraction of the OM, was relatively constant and averaged 1.8 ± 0.4 µg/g (Figure 2).

Fecal steroid concentrations (Figure 3), expressed per g of organic carbon (OC), remained consistently low for ~3,000–3,750 years, and likely represent the natural (background/wildlife) fecal material input to the lake. Cholesterol, which is present in human fecal matter but has a ubiquitous occurrence in nearly all eukaryotic cells (Volkman, 2003; Prost et al., 2017; Zocatelli et al., 2017), averaged 23.4 ± 9.3 µg/g of OC before 1900 BCE. However, at ca. 1880 BCE (95% range 2023–1738 BCE) cholesterol content increased more than sixfold to 148 µg/g of OC, with slight subsequent

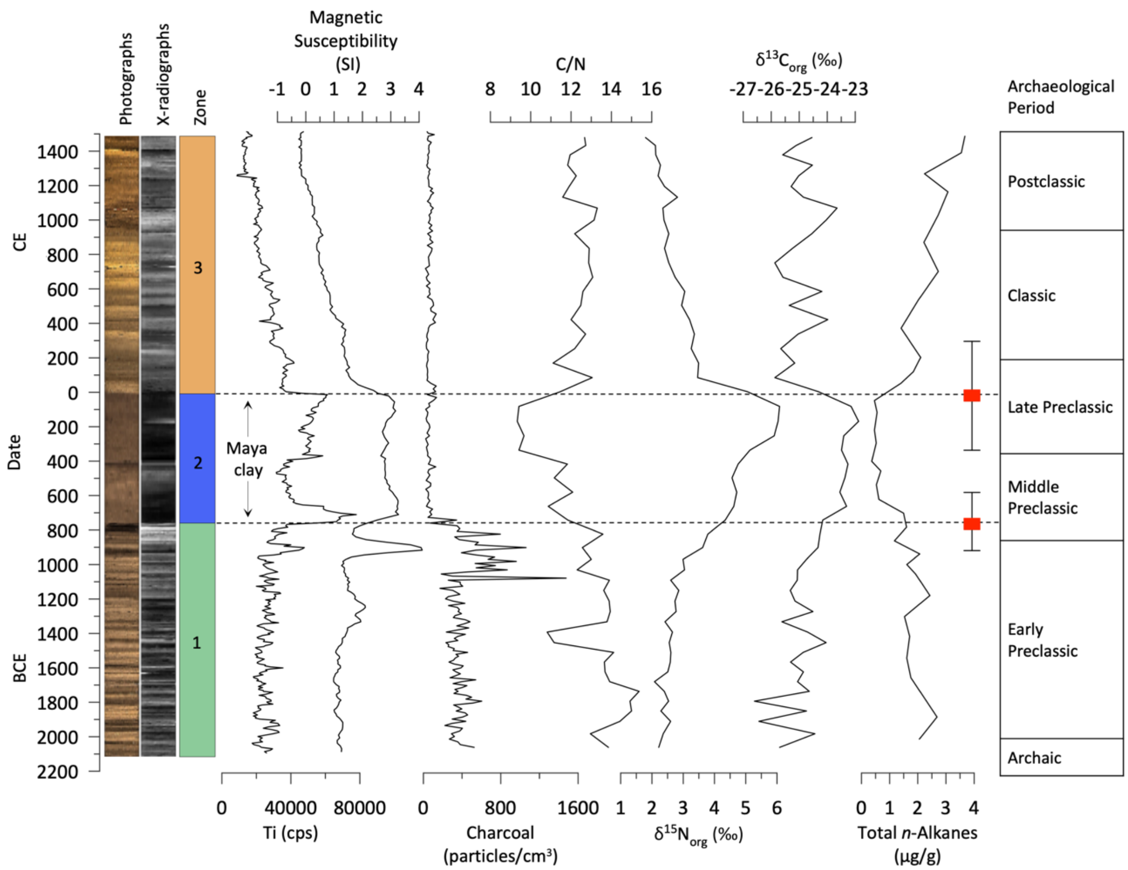

Figure 2. Titanium abundance (expressed in counts per second [cps]), magnetic susceptibility (expressed in the international system of units [SI]), charcoal abundance, C/N mass ratio, nitrogen and carbon stable isotopes of bulk organic matter, and total *n*-alkane abundance plotted against time and the corresponding archaeological periods. Date uncertainties from our age-depth model at the boundaries of Zone 2 (black dashed lines) are shown with box and whisker plots, in which the weighted means are represented by red boxes and the 95% ranges by whiskers.

increases ~1380 BCE (95% range 1466–1259 BCE) and ~960 BCE (95% range 1075–863 BCE). Cholestanol (a degradation product of cholesterol in the environment and a minor component of human fecal matter; Prost et al., 2017; Zocatelli et al., 2017) and stigmastanol (the dominant stanol of herbivore fecal matter and a constituent of human fecal matter; Prost et al., 2017) values were also consistently low before ~1900 BCE, averaging 23.1 ± 7.8 and 38.2 ± 20.1 µg/g of OC, respectively, and also displayed elevated concentrations ~1380 and ~960 BCE. Coprostanol+epicoprostanol (copro+epicopro, with coprostanol being the dominant stanol of human feces; Prost et al., 2017; Zocatelli et al., 2017) values were highly variable, averaging 25.8 ± 17.5 µg/g of OC before ~1900 BCE, with a slightly higher average of 28.5 ± 20.2 µg/g of OC after ~1900 BCE in Zone 1. Fluctuations in these organic molecules after ~1900 BCE probably serve as proxy indicators for early sparse Maya settlement of the area that became the urban center of Nixtun-Ch'ich'.

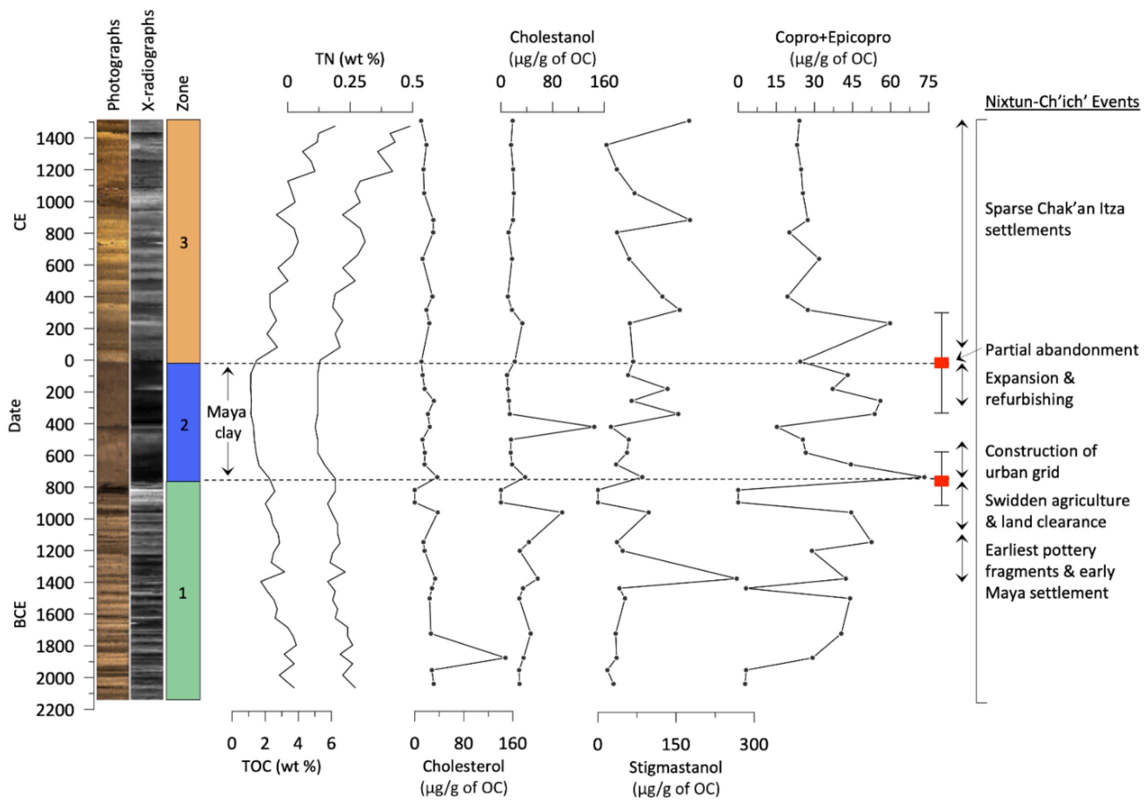

Figure 3. Total organic carbon, total nitrogen, cholesterol, cholestanol, stigmastanol, and coprostanol+epicoprostanol plotted against time. Fecal stanol/sterol concentrations are normalized to TOC. Date uncertainties from our age-depth model at the boundaries of Zone 2 (black dashed lines) are shown with box and whisker plots, in which the weighted means are represented by red boxes and the 95% ranges by whiskers.

At the bottom of Zone 1, from about 2065 to 1080 BCE, charcoal averages 359 ± 80 particles/cm^3 (Figure 2), likely representing the occurrence of both natural and anthropogenic fires in the area. At the top of Zone 1 (~1080 to ~760 BCE), charcoal increases abruptly, averaging 573 ± 308 particles/cm^3 (Figure 2). Charcoal reached a maximum of 1,476 particles/cm^3 at ~1080 BCE (95% range 1232–950 BCE), with another increase to 1,062 particles/cm^3 at ~905 BCE (95% range 1000–824 BCE). Higher-than-average charcoal abundances from ~1080 to ~760 BCE indicate high local fire activity, likely reflecting slash-and-burn agricultural practices and fire clearance of the Candelaria Peninsula by the early Maya prior to construction of Nixtun-Ch'ich'.

5.3. ZONE 2 (760–20 BCE)

Zone 2 displays distinct changes in all geochemical variables. Both TOC and TN decreased, averaging 1.4 ± 0.4 and 0.1 ± 0.03 wt%, respectively (Figure 3). These values are about half of those in Zone 1, indicating either lower primary productivity from reduced nutrient availability (e.g., Fan et al., 2017) or dilution of organic matter by enhanced clastic sedimentation (e.g., Islebe et al., 1996; Fischer et al., 2003; Enters et al., 2006). C/N ratios decreased gradually until reaching a relatively constant value of 9.5 ± 0.1 from ca. 400 to 100 BCE (Figure 2), suggesting a greater relative contribution to sediment OM from lacustrine algae (Meyers and Teranes, 2001), decomposing aquatic macrophytes (Fellerhoff et al., 2003), and/or nitrogen-rich soil OM (Talbot, 2001; Lou et al., 2012). At the same time, $\delta^{15}N_{org}$ and $\delta^{13}C_{org}$ values gradually increased until reaching highs of 6.0 ± 0.1 and -23.1 ± 0.3‰, respectively, which persisted from ca. 250 to 100 BCE (Figure 2), likely indicating increased lacustrine primary productivity (Hollander and McKenzie, 1991; Meyers and Teranes, 2001; Talbot, 2001). Total *n*-alkane abundance followed the trend observed in TOC and was relatively low, averaging 0.6 ± 0.3 µg/g (Figure 2), likely as a result of organic matter dilution within the Maya clay unit. Cholesterol values remained low in Zone 2, averaging 20.9 ± 8.4 µg/g of OC, whereas stigmastanol values were nearly double those in Zone 1 before 1900 BCE, averaging 74.4 ± 43.2 µg/g of OC, with highest concentrations registered after ~400 BC (Figure 3). Cholestanol values were low at the bottom of Zone 2, averaging 21.4 ± 10.8 µg/g of OC, but show an increase to 145 µg/g of OC at ~420 BC (Figure 3). Although highly variable, copro+epicopro values were elevated overall in Zone 2, averaging 41.6 ± 17.9 µg/g of OC, suggesting increased human fecal efflux to the lake. Charcoal concentration was also low, averaging 62 ± 49 particles/cm^3 (Figure 2), likely as a result of earlier land clearance and urbanization of the peninsula. The observed changes in lake conditions are coeval with construction and dense occupation at Nixtun-Ch'ich' (Rice, 2019; Obrist-Farner and Rice, 2019; Rice and Pugh, 2021), suggesting that soil disturbance from construction and earlier agriculture, coupled with nutrient-laden urban runoff, increased delivery of sediment and nutrients to the shallow, western arm of Lake Petén Itzá, thereby contributing to gradually intensifying eutrophication from about 760 to 20 BCE.

5.4. ZONE 3 (20 BCE–1510 CE)

The transition from Zone 2 to Zone 3 is characterized by rapid changes in all geochemical variables over a period of less than about 80 years. Throughout Zone 3, TOC and TN increased gradually, with average values of 3.6 ± 1.2 and 0.3 ± 0.1 wt%, respectively (Figure 3). C/N ratios remained relatively constant, averaging 12.4 ± 0.6

(Figure 2), suggesting sediment OM is composed of a mixture of lake algae and aquatic and land plants (Meyers and Teranes, 2001; Fellerhoff et al., 2003). Stable isotope values shifted to more negative values, with $\delta^{15}N_{org}$ and $\delta^{13}C_{org}$ averaging 2.8 ± 0.7‰ and -24.9 ± 0.7‰, respectively (Figure 2). The total *n*-alkane abundance increased gradually, following the trend of TOC, averaging 2.4 ± 0.7 µg/g (Figure 2). Cholesterol and cholestanol values were low, averaging 19.5 ± 7.7 and 18.4 ± 5.9 µg/g of OC, respectively (Figure 3). These concentrations are similar to those observed in Zone 1 before ~1900 BCE, indicating a decline in fecal contamination. Stigmastanol, however, was higher on average, with a concentration of 89.1 ± 58.5 µg/g of OC, and fluctuated throughout Zone 3, with peaks between ~160 and 180 µg/g of OC at ~320 CE, ~880 CE, and ~1510 CE (Figure 3), suggesting sustained, sporadic periods of greater herbivorous fecal input to the lake (Prost et al., 2017; Keenan et al., 2021). Copro+epicopro values were low in Zone 3, averaging 28.0 ± 11.1 µg/g of OC, which is similar to the average observed in Zone 1 after ~1900 BC and indicates a decline in human fecal contamination. Charcoal concentrations in Zone 3 remained low and similar to those in Zone 2, averaging 63 ± 24 particles/cm^3 (Figure 2), suggesting continued low local fire activity after construction of the city.

6. DISCUSSION

Our data highlight a previously unrecognized period of substantial human disturbance in Lake Petén Itzá between ca. 760 and 20 BCE. Archaeological findings suggest substantial population growth at Nixtun-Ch'ich' during the Middle Preclassic

(900/800–400/300 BCE; Rice, 2019), coincident with our paleolimnological evidence of trophic state changes in the western arm of the lake. We infer relatively pristine (oligotrophic) and stable lake conditions in the older part of our sediment record, prior to the period of archaeologically documented human disturbance. Only slight changes in lake conditions were recorded near the end of the Early Preclassic, when early Maya land cover changes began ca. 1100 BCE, several hundred years before establishment of the site's urban grid from about 800 to 500 BCE (Pugh and Rice, 2017; Pugh, 2019; Obrist-Farner and Rice, 2019). Increasing charcoal abundance from ca. 1080 to 760 BCE records a greater number of fire events in the catchment of the western arm of the lake and marks the earliest human-mediated burning at this location, suggesting the ancient Maya were well established on the Candelaria Peninsula and in surrounding areas by the end of the Early Preclassic. Temporal coincidence of increased charcoal abundance in core PI-NC-1 (Figure 2) with the first appearance of corn (*Zea mays*) pollen in the northern basin of Lake Petén Itzá (~1,050 BCE; Mueller et al., 2009) points to the early use of swidden agricultural practices by Maya populations around the lake, and perhaps by the early Maya that constructed platform ZZ1 at the eastern end of the Peninsula in the late Early Preclassic period (pre-1000/900 BCE; Rice, 2009). Mueller et al. (2009) also reported increases in pollen of disturbance taxa (*Asteraceae*, *Ambrosia*, and *Chenopodiaceae*) from about 1050 BCE to 950 CE, providing supporting evidence for Maya land clearance beginning in the late Early Preclassic. Additionally, our fecal steroid data (increases in cholesterol, cholestanol, and stigmastanol, and higher average copro+epicopro; Figure 3), along with an early increase in sediment magnetic susceptibility (Figure 2), support an inference for early, albeit sparse, Maya settlement at the site of Nixtun-Ch’ich’ during the late Early Preclassic, beginning ca. 1400–1300 BCE (K’as Ceramic Complex; Rice, 2019).

Several distinct changes in the sediment occur beginning ca. 760 BCE, during development of Nixtun-Ch’ich’. Sedimentological changes indicate a rapid shift in lake and catchment conditions leading to the appearance of a relatively thin layer of the Maya clay at this site throughout most of the Middle and Late Preclassic periods (ca. 800 BCE–200 CE). Paleolimnological studies in several smaller central Petén lakes suggested that forest clearance and urban construction led to rapid soil erosion and siltation of water bodies, in some cases leading to deposition of Maya clay units that are several meters thick (Deevey et al., 1979; Binford et al., 1987, Brenner et al., 2002, Anselmetti et al., 2007). In the eastern arm of Lake Petén Itzá’s southern basin, however, the Maya clay, which spanned approximately 1,700 years, did not appear as an obvious, distinct unit and could only be identified with geochemical and magnetic susceptibility records (Curtis et al., 1998), demonstrating that Maya clay deposition was heterogeneous across the Petén lakes. In our core from the western arm of the lake’s southern basin, the Maya clay is ~0.5 m thick and spans only about 800 years. Higher Ti abundance and an increase in magnetic susceptibility beginning ca. 760 BCE (Obrist-Farner and Rice, 2019; Figure 2) likely reflect highly localized erosional signals caused by human activities at Nixtun-Ch’ich’ (e.g., grid establishment and maintenance; Obrist-Farner and Rice, 2019), rather than more widespread changes in the lake catchment (e.g., deforestation). The relatively thin nature and short time span of the Maya clay unit at our core site might suggest that severe siltation did not prevail in the shallow, southern basin of Lake Petén Itzá during the Middle and Late Preclassic.

The initiation of gradual increases in $\delta^{15}N_{org}$ and $\delta^{13}C_{org}$, with a simultaneous gradual decline in the C/N ratio, coincided with an abrupt increase in local fire activity ca. 1080 BCE, as inferred from the charcoal record (Figure 2). Local fires related to swidden agricultural practices likely caused pulses of soil erosion (and consequent sediment deposition in the lake) that delivered greater nutrient loads and terrestrial material to the waterbody, thereby altering lake conditions. For example, higher titanium and magnetic susceptibility values ca. 905 BCE (Figure 2; Obrist-Farner and Rice, 2019) correspond with charcoal evidence for a large fire event that also marks the beginning of more pronounced changes in organic matter constituents. By the time construction of the urban grid in Nixtun-Ch'ich' began ca. 760 BCE (Obrist-Farner and Rice, 2019), increasing values of both $\delta^{13}C_{org}$ and $\delta^{15}N_{org}$, and declining C/N ratios (Figure 2), indicate greater contributions of algal and/or decomposing aquatic macrophyte OM to the sediment (Meyers and Teranes, 2001; Fellerhoff et al., 2003; Inglett and Reddy, 2006), which were sustained through Late Preclassic Maya occupation, suggesting intensifying cultural eutrophication in the shallow waters adjacent to Nixtun-Ch'ich' during the Middle and Late Preclassic. Nitrogen and carbon stable isotope enrichment support an inference for eutrophication as initially aquatic primary producers preferentially utilize the lighter carbon (^{12}C) and nitrogen (^{14}N) isotopes during photosynthesis and protein synthesis, respectively, but as those reservoirs are progressively depleted, algae and macrophytes are forced to incorporate the heavier isotopes (^{13}C and ^{15}N) and thus become isotopically enriched (Hollander and McKenzie, 1991; Meyers and Teranes, 2001; Talbot, 2001; Inglett and Reddy, 2006). Short-chain (C_{17}–C_{21}) alkane abundances, which are generally produced by aquatic algae and microbes (Cranwell et al., 1987; Berke, 2018), were low in core PI-NC-1 (Figure S5 in Supplementary Information), potentially suggesting low rates of primary production in the lake, but this was also observed throughout an 85 ky record in Lake Petén Itzá, instead suggesting that short-chain alkanes may not be produced in large quantities or are not well preserved in the lake (Mays et al., 2017). Alkane abundances are instead dominated by long-chain (C_{29}–C_{35}) *n*-alkanes (Figure S5 in Supplementary Information), which are generally interpreted to represent a dominant terrestrial source (Berke, 2018), but some emergent macrophytes also produce large quantities of long-chain *n*-alkanes (Ficken et al., 2000) and likely contribute to the predominance of long-chain alkanes in core PI-NC-1 as emergent macrophytes are prevalent along the modern shoreline of the Candelaria Peninsula in Lake Petén Itzá.

There are, however, possible alternative explanations for the stratigraphic shifts displayed by some variables. For example, an increase in $\delta^{13}C_{org}$ can also indicate a shift to a greater relative contribution to sediment OM from C_4 (maize and other tropical grasses) versus C_3 (woody trees and shrubs) vegetation (Huang et al., 2001; Mueller et al., 2009; Wright et al., 2019), but C/N ratios in core PI-NC-1 are inconsistent with those of C_4 vegetation (Figure S3 in Supplementary Information; Meyers and Teranes, 2001), and changes in $\delta^{13}C_{org}$ do not correlate with initial forest decline beginning ca. 2550 BCE (Mueller et al., 2009) or abrupt increases in pollen from disturbance taxa ca. 1050 BCE (Mueller et al., 2009) or charcoal ca. 1080 BCE, which likely reflect early maize cultivation at this location. Additionally, given inferred reduction of riparian vegetation in the catchment after ca. 760 BCE, reduced terrestrial OM input to the lake could have increased the relative proportion of lacustrine OM in sediments, even with constant lacustrine primary productivity, yielding a false eutrophication signal. However, if this were the case, shifts in OM proxies would likely persist through the Classic Period until forest recovery ca. 900–1200 CE (Islebe et al., 1996; Mueller et al., 2010). Furthermore, enhanced sewage input to the lake could also cause an increase in $\delta^{15}N_{org}$ (Meyers and Teranes, 2001; Talbot, 2001), corresponding with increased average copro+epicopro content in the lake sediments (Figure 3). Declining C/N ratios with corresponding increases in $\delta^{15}N_{org}$ could also be explained by increases in delivery of nitrogen-rich and ^{15}N-enriched soil OM to the lake (Talbot, 2001; Lou et al., 2012), as a consequence of soil erosion driven by fires and construction activities in the catchment.

However, synchronous enrichment of $\delta^{15}N_{org}$ and $\delta^{13}C_{org}$, with a corresponding decline in the C/N ratio (Figure 2), suggest a singular controlling mechanism, which is most parsimoniously explained by greater lacustrine primary productivity. The gradual changes in OM measures ($\delta^{15}N_{org}$, $\delta^{13}C_{org}$, and C/N ratios) are inconsistent with the abrupt onset of both increased fire activity ca. 1080 BCE and enhanced clastic sedimentation related to the establishment of the urban grid ca. 760 BCE (Obrist-Farner and Rice, 2019). This suggests that the proxies reflect a progressive change in lake conditions rather than a shift in the source of terrestrial OM input (i.e., terrestrial vegetation, soil organics) to the lake. Furthermore, our interpretation for increased primary productivity is supported by similarities in organic matter proxies from Zone 2 with recent data, when the lake is known to have experienced eutrophication (Figure S4 in Supplementary Information; Rosenmeier et al., 2004; Pérez et al., 2010). Although eutrophication typically leads to increases in TOC and TN, low values for these measures within the Maya clay unit are likely the result of mineral dilution (e.g., Islebe et al., 1996; Fischer et al., 2003; Enters et al., 2006), thereby masking the environmental signal of eutrophication. A similar trend is observed in the total *n*-alkane abundance (Figure 2), supporting an inference for dilution of OM in Zone 2.

Maximum eutrophic conditions, inferred from increases in both $\delta^{13}C_{org}$ and $\delta^{15}N_{org}$, and a decline in C/N ratios, appear to have lasted about 300 years, from ~400 to 100 BCE, and coincided with dense occupation at Nixtun-Ch’ich’ and the enlargement of several monumental structures during the Late Preclassic (Pugh, 2019). Eutrophication of the western arm of the lake was likely driven primarily by effluxes of soil phosphorus to the lake, first due to the removal of vegetation that had previously anchored soil in the catchment and the use of slash-and-burn agricultural practices, and then as a result of construction events in the city. Nutrient loading from fecal material derived from the peninsula, as evinced by a high average copro+epicopro concentration, the highest cholestanol concentration ca. 420 BCE, and elevated stigmastanol concentrations in the Late Preclassic, may have also fueled lacustrine primary productivity in the lake. Additional inputs of nutrients from food wastes that accumulated in Preclassic ritual middens in Nixtun-Ch’ich’ (Rice and Pugh, 2017) may have contributed to lake eutrophication during the Late Preclassic but was likely not a dominant factor.

Previous studies of Petén lake sediment cores did not detect evidence of ancient, Maya-mediated cultural eutrophication. Several factors may have facilitated cultural eutrophication at our study site: 1) shallow water depths (8.4 m water depth at the coring site and generally less than 10 m in the area; Hodell et al., 2006) in the western arm of Lake Petén Itzá, enabling high concentrations of nutrients in the water column; 2) poor hydrologic exchange of water between the western arm and the rest of the lake (i.e. long water residence time and limited nutrient dilution); 3) proximity of Nixtun-Ch’ich’ to the lake shore, which promoted drainage of nutrient-laden runoff from the city to the lake; 4) design of the streets, avenues, and canals in Nixtun-Ch'ich', which were paved with plaster and/or limestone flagstones (Pugh and Rice, 2017; Rice and Pugh, 2021; Pugh et al., in press) and likely expedited delivery of nutrient-rich runoff to the western arm of the lake; and 5) minimal presence of riparian vegetation to anchor surficial soils, as revealed by low abundances of charcoal beginning in the Middle Preclassic. Watershed deforestation is also supported by Schüpbach et al. (2015), who attributed a shift to low fire activity ca. 450 BCE to earlier human-mediated forest reduction and consequent grassland expansion. In our sediment core collected near the Candelaria Peninsula, however, low charcoal counts after ~760 BCE are likely the result of urbanization (i.e., construction and occupation of Nixtun-Ch'ich'), which would have limited local forest recovery and enhanced nutrient delivery through soil erosion during dense Preclassic occupation of the city. Land clearance and urbanization limited fuel availability for fires and charcoal production and mark a human-induced shift from a high- to low-severity local fire regime on the Candelaria Peninsula.

Our sediment core study, when coupled with information from archaeological excavations, sheds light on the environmental consequences of ancient Maya settlement on lake trophic status. Archaeological excavations at Nixtun-Ch'ich' show little evidence of Early Classic (250–600 CE) occupation (Pugh and Rice, 2017), suggesting a population decline in the Maya city during the Terminal Preclassic (ca. 100–250 CE), potentially due to changes in climatic conditions (Obrist-Farner and Rice, 2019). Archaeological investigations have also found evidence for changes in Maya fishing practices at Nixtun-Ch'ich' during the Terminal Preclassic (Rice et al., 2017), which hint at changing lake conditions and likely reflect a human response to changing trophic status. Population decline and partial or temporary Late to Terminal Preclassic abandonment of the city coincides with ameliorating conditions in the lake, which occurred over a period of ≤ 80 years (ca. 20 BCE to 60 CE), potentially suggesting that population decline occurred rapidly. Rapid return of C/N, $\delta^{13}C_{org}$, and $\delta^{15}N_{org}$ to values similar to those in the lower part of the record, combined with statistical similarity of both $\delta^{13}C_{org}$ and C/N ratios in Zones 1 and 3 (Figure 4), indicate that the western arm of Lake Petén Itzá recovered and reached stable limnological conditions ca. 60 CE (95% range 257 BCE–376 CE), after the cessation of construction activities and dense human occupation (Obrist-Farner and Rice, 2019) ca. 20 BCE (95% range 334 BCE–298 CE; Figure 2). Nevertheless, results suggest that the extent of lake recovery was limited and did not return to its pre-disturbance state, as C/N ratios in Zone 3 are lower than those in Zone 1 and remain similar to those in Zone 2 (Figure 4). Consistent geochemical measures after ~60 CE, combined with persistent low charcoal abundance, indicate reduced Maya disturbance and decreased soil erosion, perhaps a result of the city's corridors having been plastered over by the beginning of the Classic period (Pugh and Rice, 2017). Occupation of Nixtun-Ch'ich' and its environs during the Classic and Postclassic (Rice, 2018) by dispersed, small settlements of Chak'an Itzas (Pugh et al., 2016) may have contributed to the limited recovery of the western arm of Lake Petén

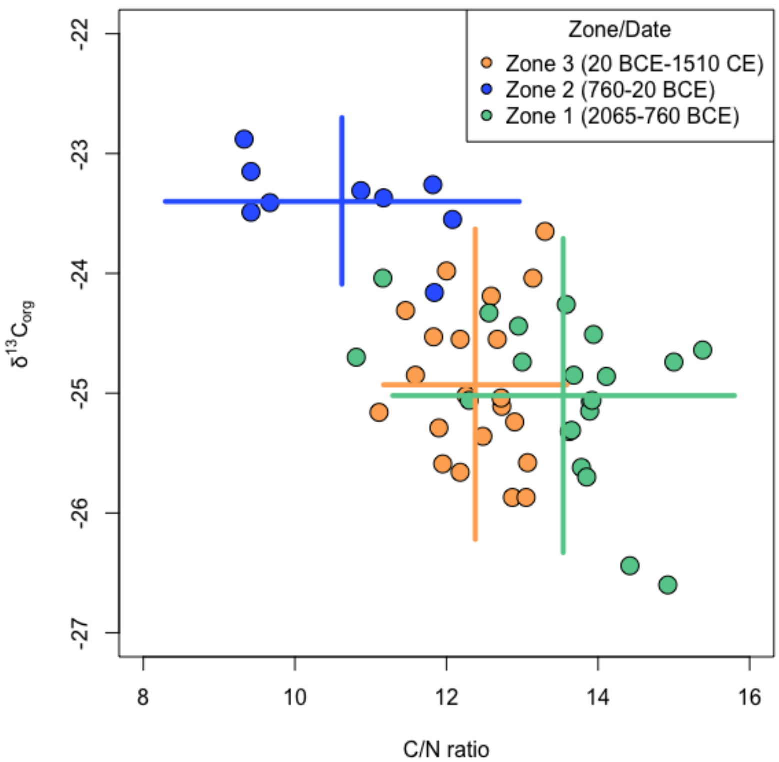

Figure 4. Lake Petén Itzá C/N mass ratios and $\delta^{13}C_{org}$ by zone. Crosses indicate 2 standard deviation (2σ) ranges.

Itzá. Fluctuations in stigmastanol concentrations suggest occasional pulses of fecal material from large herbivores, such as deer and tapirs (Prost et al., 2017; Sharpe et al., 2018), potentially as a result of sporadic human population declines (e.g., Keenan et al., 2021) or migration, suggesting population variability during the Classic and Postclassic. Low copro+epicopro concentrations throughout most of the Classic and Postclassic periods, however, also suggest that Chak'an Itza populations were consistently small relative to Preclassic populations. In any case, sustained, low-level Maya occupation of Nixtun-Ch'ich' during the Classic and Postclassic appears to have prevented full recovery of the lake to pre-disturbance trophic state conditions, after almost 800 years of cultural eutrophication.

APPENDIX

SUPPLEMENTARY FIGURES AND TABLES

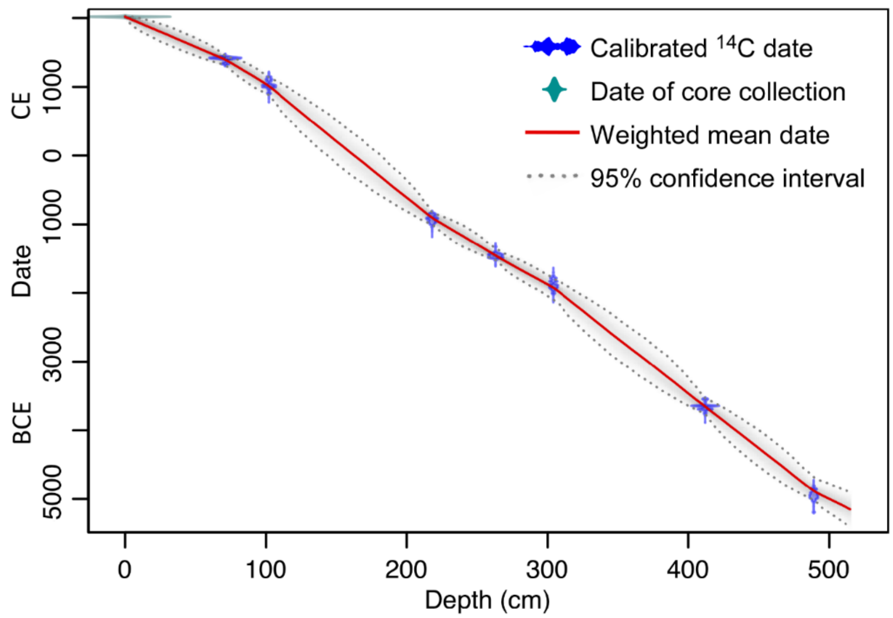

Figure S1. Age-depth model created using the Bayesian software Bacon (rbacon package in R; Blaauw and Christen, 2011) based on seven radiocarbon ages (blue) and the date the core was retrieved (green). Radiocarbon ages were calibrated using IntCal20 (for northern hemisphere terrestrial radiocarbon dates; Reimer et al., 2020). Solid red line shows weighted mean date, and dotted gray envelope shows the 95% range of probable dates.

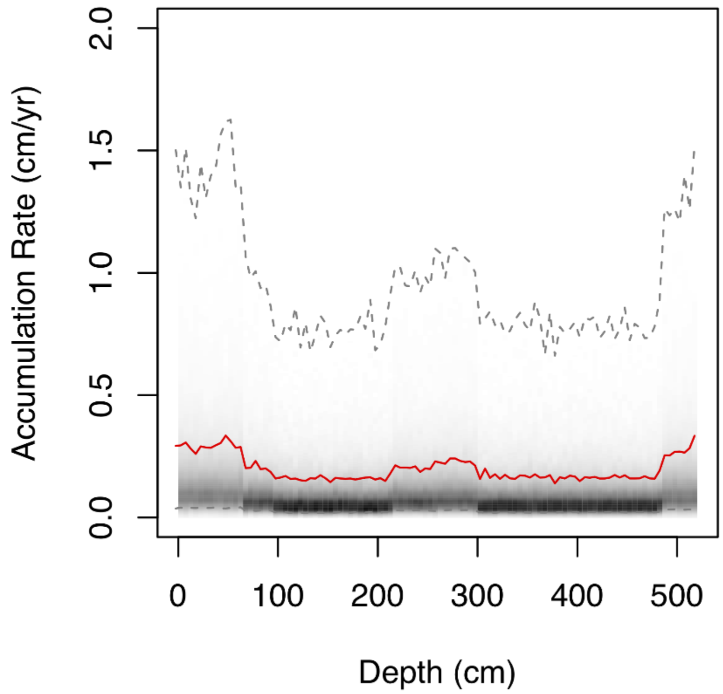

Figure S2. Approximate sediment accumulation rates in cm/yr in Lake Petén Itzá core PI-NC-1, created using the Bayesian software Bacon (rbacon package in R; Blaauw and Christen, 2011). Solid red line shows mean accumulation rate, and dashed gray envelope shows the 95% range. Zone 2 (Maya clay) ranges from 164 to 209 cm.

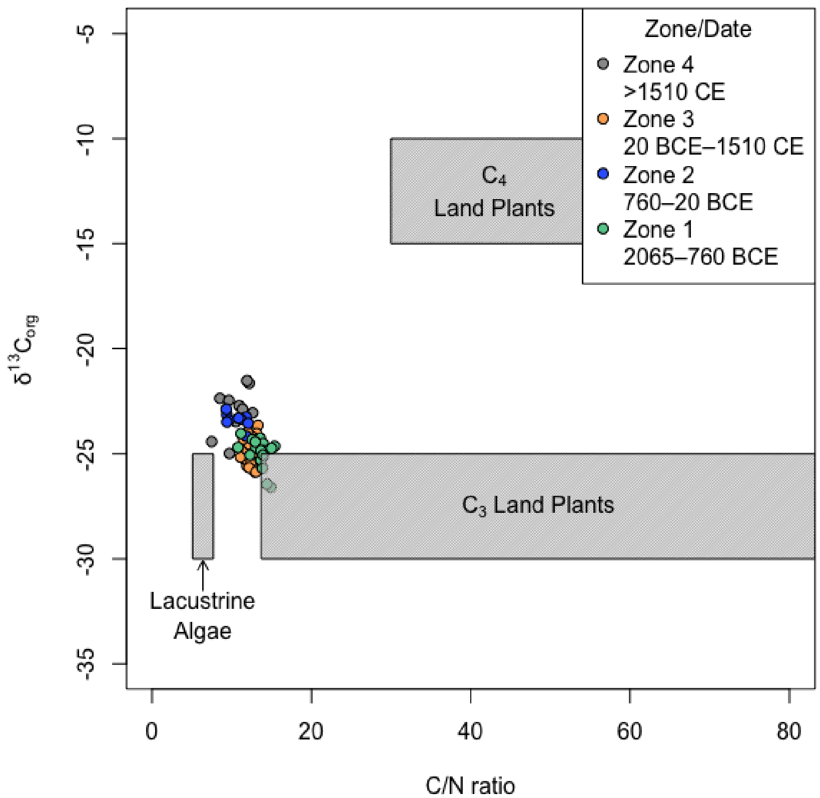

Figure S3. Lake Petén Itzá C/N mass ratios and $\delta^{13}C_{org}$ values plotted against typical values from various organic matter sources (modified from Meyers and Teranes, 2001).

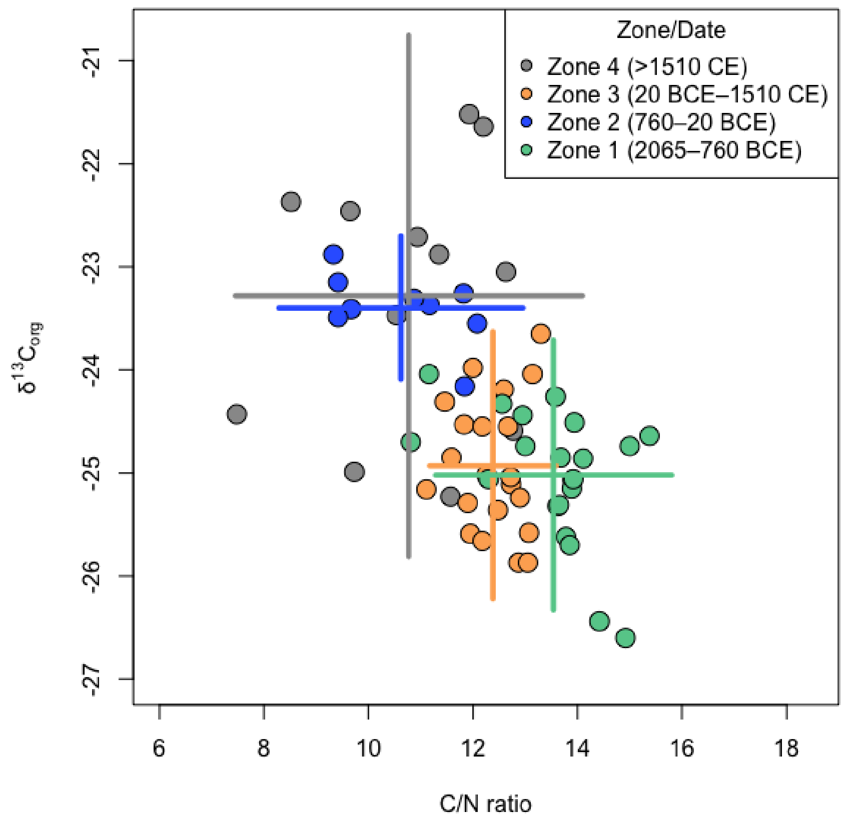

Figure S4. Lake Petén Itzá C/N mass ratios and $\delta^{13}C_{org}$ by zone. Crosses represent the 2 standard deviation (2σ) ranges for each zone. The means of C/N mass ratios and $\delta^{13}C_{org}$ in Zones 2 and 4 are statistically similar, although Zone 4 has higher variance. Similarities between recent data (Zone 4), when the lake is known to have experienced eutrophication (Rosenmeier et al., 2004; Pérez et al., 2010), and Zone 2, during dense Maya occupation of Nixtun-Ch'ich', suggest that the lake underwent similar changes at each time, both of which were driven by anthropogenic land-use changes.

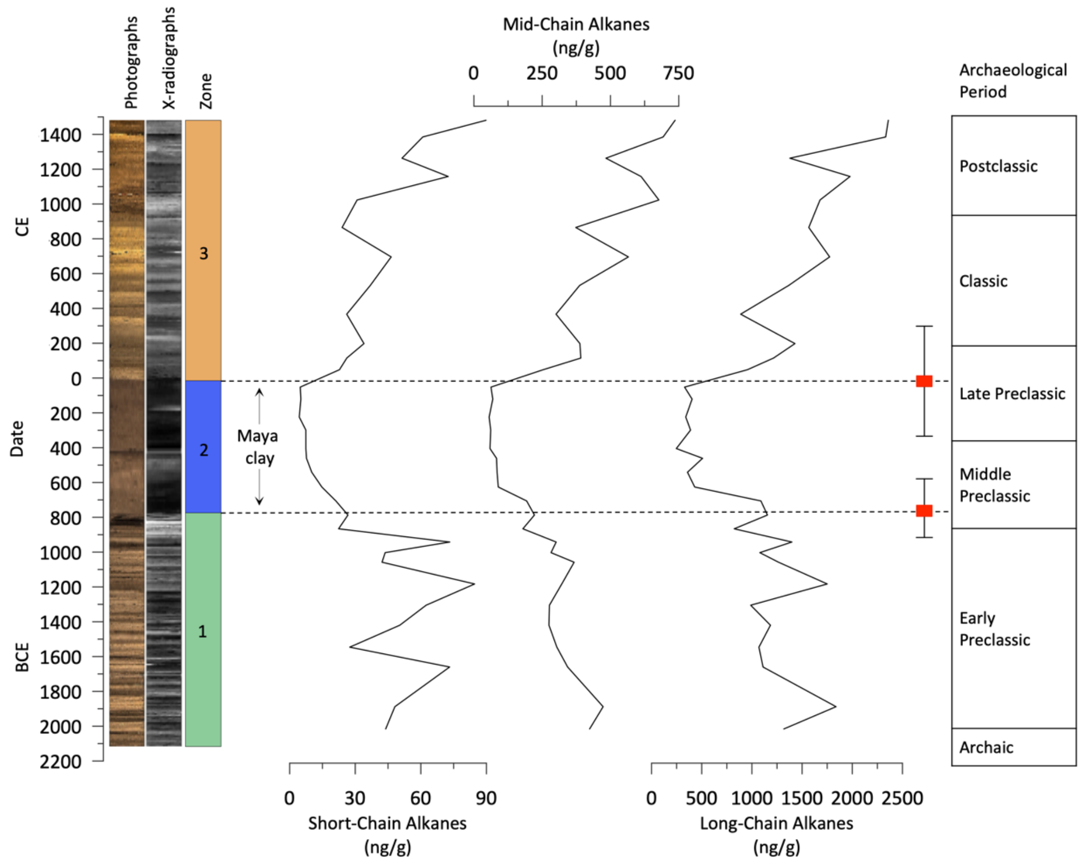

Figure S5. Short-chain (C_{17}–C_{21}), mid-chain (C_{23}–C_{27}), and long-chain (C_{29}–C_{35}) *n*-alkane abundances plotted against time and the corresponding archaeological periods. Date uncertainties from our age-depth model at the boundaries of Zone 2 (black dashed lines) are shown with box and whisker plots, in which the weighted means are represented by red boxes and the 95% ranges by whiskers. The abundances of all alkane chain lengths decreased in Zone 2 (Maya clay).

Table S1. Calibrated radiocarbon dates on wood charcoal from Lake Petén Itzá core PI-NC-1 (modified from Obrist-Farner and Rice, 2019).

Lab ID	Sample ID	Depth (cm)	^{14}C Age	Calibrated Mean Date*	Calibrated Date Range (2σ)*
180979	PI-1-1	71	515 ± 30	1397 CE	1314–1446 CE
180980	PI-1-2	102	1020 ± 40	1009 CE	887–1138 CE
185399	PI-218	218	2775 ± 30	905 BCE	1000–824 BCE
180981	PI-1-3	263	3190 ± 30	1456 BCE	1519–1344 BCE
180982	PI-1-4	304	3550 ± 35	1925 BCE	2094–1791 BCE
180983	PI-1-5	412	4875 ± 30	3659 BCE	3770–3536 BCE
180984	PI-1-6	489	6050 ± 35	4878 BCE	5014–4661 BCE

*Modeled using the Bayesian software Bacon (rbacon package in R; Blaauw and Christen, 2011) and calibrated using IntCal20 (for northern hemisphere terrestrial radiocarbon dates; Reimer et al., 2020)

Table S2. Sample means and 2 standard deviation (2σ) ranges for C/N mass ratios and $\delta^{13}C_{org}$ in Zones 1–4.

Zone	Date	C/N mass ratios			$\delta^{13}C_{org}$ (‰)		
		-2σ	mean	+2σ	-2σ	mean	+2σ
Zone 4	>1510 CE	7.46	10.77	14.09	-25.81	-23.28	-20.75
Zone 3	20 BCE–1510 CE	11.17	12.38	13.59	-26.22	-24.93	-23.63
Zone 2	760–20 BCE	8.29	10.62	12.96	-24.09	-23.40	-22.70
Zone 1	2065–760 BCE	11.29	13.54	15.80	-26.33	-25.02	-23.71

Table S3. Titanium abundance (from x-ray fluorescence core scanning) and magnetic susceptibility (Obrist-Farner and Rice, 2019), geochemical data, total *n*-alkane abundances, fecal sterol/stanol abundances normalized to TOC, and charcoal abundances from Lake Petén Itzá core PI-NC-1.

Depth (cm)	Age (cal yr BP)	Date (BCE/CE)	Ti (cps)	MS (SI)	TOC (wt %)	TN (wt %)	C/N mass ratio	$\delta^{15}N_{org}$ (‰)	$\delta^{13}C_{org}$ (‰)	Total *n*-alkanes (µg/g)	Cholesterol (µg/g of OC)	Cholestanol (µg/g of OC)	Stigmastanol (µg/g of OC)	Coprostanol + Epicoprostanol (µg/g of OC)	Charcoal (particles/ cm^3)
0	-68	2018									30.33	22.94	32.80	4.86	
0.5	-64	2014													
1	-59	2009													9
1.5	-55	2005													
2	-51	2001													
2.5	-46	1996													
3	-42	1992			9.35	1.25	7.48	2.29	-24.43						7
3.5	-38	1988													
4	-33	1983													
4.5	-29	1979													
5	-25	1975													6
5.5	-21	1971													
6	-16	1966													
6.5	-12	1962													
7	-8	1958													19
7.5	-3	1953									27.20	55.04	75.08	7.25	
8	1	1949													
8.5	5	1945													
9	10	1940			7.41	0.87	8.52	1.94	-22.37						16
9.5	14	1936													
10	18	1932													
10.5	23	1927													
11	27	1923													23
11.5	31	1919													
12	36	1914													
12.5	40	1910													
13	44	1906			7.91	0.82	9.65	1.29	-22.46	3.61					13
13.5	49	1901													
14	53	1897													
14.5	57	1893													
15	62	1888													14
15.5	66	1884													
16	71	1879									59.26	65.88	92.63	53.75	
16.5	75	1875													
17	80	1870													11
17.5	84	1866													
18	89	1861													

Table S3. Titanium abundance (from x-ray fluorescence core scanning) and magnetic susceptibility (Obrist-Farner and Rice, 2019), geochemical data, total *n*-alkane abundances, fecal sterol/stanol abundances normalized to TOC, and charcoal abundances from Lake Petén Itzá core PI-NC-1. (Cont.)

Depth (cm)	Age (cal yr BP)	Date (BCE/CE)	Ti (cps)	MS (SI)	TOC (wt %)	TN (wt %)	C/N mass ratio	$\delta^{15}N_{org}$ (‰)	$\delta^{13}C_{org}$ (‰)	Total *n*-alkanes (μg/g)	Cholesterol (μg/g of OC)	Cholestanol (μg/g of OC)	Stigmastanol (μg/g of OC)	Coprostanol + Epicoprostanol (μg/g of OC)	Charcoal (particles/ cm^3)
18.5	93	1857													
19	98	1852			9.24	0.95	9.73	1.33	-24.99						25
19.5	102	1848													
20	107	1843													
20.5	111	1839													
21	115	1835													12
21.5	120	1830													
22	124	1826													
22.5	129	1821													
23	133	1817			7.8	0.74	10.54	1.13	-23.47	3.14					18
23.5	137	1813													
24	142	1808													
24.5	146	1804									16.09	12.64	28.82	32.48	
25	150	1800													22
25.5	155	1795													
26	159	1791													
26.5	163	1787													
27	167	1783													11
27.5	171	1779													
28	176	1774													
28.5	180	1770													
29	184	1766			6.89	0.63	10.94	1.03	-22.71						8
29.5	188	1762													
30	193	1757													
30.5	197	1753													
31	201	1749													19
31.5	206	1744													
32	210	1740													
32.5	214	1736													
33	218	1732			7.38	0.65	11.35	1.15	-22.88	2.61	12.58	20.03	54.55	25.81	18
33.5	223	1727													
34	227	1723													
34.5	231	1719													
35	236	1714													10
35.5	240	1710													
36	244	1706													
36.5	248	1702													

Table S3. Titanium abundance (from x-ray fluorescence core scanning) and magnetic susceptibility (Obrist-Farner and Rice, 2019), geochemical data, total *n*-alkane abundances, fecal sterol/stanol abundances normalized to TOC, and charcoal abundances from Lake Petén Itzá core PI-NC-1. (Cont.)

Depth (cm)	Age (cal yr BP)	Date (BCE/CE)	Ti (cps)	MS (SI)	TOC (wt %)	TN (wt %)	C/N mass ratio	$\delta^{15}N_{org}$ (‰)	$\delta^{13}C_{org}$ (‰)	Total *n*-alkanes (µg/g)	Cholesterol (µg/g of OC)	Cholestanol (µg/g of OC)	Stigmastanol (µg/g of OC)	Coprostanol + Epicoprostanol (µg/g of OC)	Charcoal (particles/ cm^3)
37	253	1697													23
37.5	257	1693													
38	261	1689													
38.5	266	1684													
39	270	1680			10.07	0.87	11.57	1.56	-25.23						20
39.5	274	1676													
40	278	1672													
40.5	283	1667													
41	287	1663													22
41.5	291	1659													
42	296	1654													
42.5	300	1650													
43	304	1646			6.71	0.55	12.2	1.14	-21.64	2.70					26
43.5	308	1642													
44	313	1637													
44.5	317	1633													
45	321	1629													22
45.5	326	1624													
46	330	1620													
46.5	334	1616													
47	339	1611													12
47.5	343	1607													
48	347	1603													
48.5	352	1598													
49	356	1594			6.56	0.55	11.93	1.01	-21.52						21
49.5	360	1590													
50	365	1585									11.24	16.28	0.00	19.30	40
50.5	369	1581	9104												
51	374	1576	10579												30
51.5	378	1572	11781												
52	382	1568	12423	-0.1661						3.46					36
52.5	386	1564	14137												
53	391	1559	17153	-0.2721	7.28	0.57	12.77	1.56	-24.59						47
53.5	395	1555	18406												
54	399	1551	15779	-0.2623											43
54.5	404	1546	15141												
55	408	1542	16323	-0.2709											78

Table S3. Titanium abundance (from x-ray fluorescence core scanning) and magnetic susceptibility (Obrist-Farner and Rice, 2019), geochemical data, total *n*-alkane abundances, fecal sterol/stanol abundances normalized to TOC, and charcoal abundances from Lake Petén Itzá core PI-NC-1. (Cont.)

Depth (cm)	Age (cal yr BP)	Date (BCE/CE)	Ti (cps)	MS (SI)	TOC (wt %)	TN (wt %)	C/N mass ratio	$\delta^{15}N_{org}$ (‰)	$\delta^{13}C_{org}$ (‰)	Total *n*-alkanes (μg/g)	Cholesterol (μg/g of OC)	Cholestanol (μg/g of OC)	Stigmastanol (μg/g of OC)	Coprostanol + Epicoprostanol (μg/g of OC)	Charcoal (particles/ cm^3)
55.5	412	1538	15850												
56	417	1533	15293	-0.1822											45
56.5	421	1529	17242												
57	426	1524	16657	-0.1777											29
57.5	430	1520	16995												
58	434	1516	15063	-0.1748	5.05	0.4	12.63	1.82	-23.05						47
58.5	439	1511	14073												
59	443	1507	14371	-0.0846							10.34	18.19	175.05	24.07	39
59.5	447	1503	15451												
60	452	1498	15196	-0.1754											50
60.5	456	1494	15828												
61	460	1490	16605	-0.1866											113
61.5	464	1486	17539												
62	469	1481	17395	-0.1839						3.67					50
62.5	473	1477	15476												
63	477	1473	14008	-0.1747	6.21	0.49	12.67	1.79	-24.55						48
63.5	481	1469	14556												
64	486	1464	13293	-0.2483											42
64.5	490	1460	12855												
65	494	1456	12281	-0.1617											46
65.5	499	1451	11619												
66	504	1446	13202	-0.1577											81
66.5	508	1442	13052												
67	513	1437	12119	-0.1627											72
67.5	518	1432	11889												
68	523	1427	11758	-0.1649	5.22	0.41	12.73	2.11	-25.11						56
68.5	527	1423	12020												
69	532	1418	14396	-0.2448											57
69.5	537	1413	14640												
70	542	1408	14199	-0.1562											54
70.5	548	1402	13800												
71	553	1397	13784	-0.1581											60
71.5	559	1391	13570												
72	565	1385	13277	-0.1642						3.55					58
72.5	571	1379	13711												
73	577	1373	13326	-0.1573	5.14	0.43	11.95	2.12	-25.59						45
73.5	583	1367	12560												

Table S3. Titanium abundance (from x-ray fluorescence core scanning) and magnetic susceptibility (Obrist-Farner and Rice, 2019), geochemical data, total *n*-alkane abundances, fecal sterol/stanol abundances normalized to TOC, and charcoal abundances from Lake Petén Itzá core PI-NC-1. (Cont.)

Depth (cm)	Age (cal yr BP)	Date (BCE/CE)	Ti (cps)	MS (SI)	TOC (wt %)	TN (wt %)	C/N mass ratio	$\delta^{15}N_{org}$ (‰)	$\delta^{13}C_{org}$ (‰)	Total *n*-alkanes (µg/g)	Cholesterol (µg/g of OC)	Cholestanol (µg/g of OC)	Stigmastanol (µg/g of OC)	Coprostanol + Epicoprostanol (µg/g of OC)	Charcoal (particles/ cm^3)
74	589	1361	12772	-0.1562											51
74.5	595	1355	12699								19.04	15.68	16.34	23.15	
75	601	1349	12595	-0.1583											50
75.5	607	1343	13239												
76	613	1337	12836	-0.157											43
76.5	619	1331	13120												
77	625	1325	14014	-0.2333											47
77.5	631	1319	13712												
78	637	1313	13238	-0.1615	4.26	0.36	11.83	2.27	-24.53						35
78.5	644	1306	12684												
79	650	1300	13113	-0.2303											43
79.5	656	1294	12625												
80	662	1288	14016	-0.1558											71
80.5	668	1282	13048												
81	674	1276	13147	-0.1563											57
81.5	681	1269	15187												
82	687	1263	14131	-0.1525						2.24					62
82.5	693	1257	9015												
83	699	1251	8767	-0.1492	4.78	0.39	12.26	2.2	-25.02						51
83.5	706	1244													
84	712	1238	20179												46
84.5	718	1232	17107	0											
85	724	1226	17978												54
85.5	730	1220	19461	0											
86	737	1213	19001												56
86.5	743	1207	18416	0											
87	749	1201	18696								14.30	18.96	36.11	24.75	57
87.5	755	1195	18366	0.0795											
88	761	1189	18396		5	0.42	11.9	2.4	-25.29						57
88.5	767	1183	21522	0.0788											
89	773	1177	20273												94
89.5	779	1171	20519	0.0786											
90	786	1164	21669												72
90.5	792	1158	20257	0.1566						3.07					
91	798	1152	19757												106
91.5	804	1146	19776	0.157											
92	810	1140	19266												81

Table S3. Titanium abundance (from x-ray fluorescence core scanning) and magnetic susceptibility (Obrist-Farner and Rice, 2019), geochemical data, total *n*-alkane abundances, fecal sterol/stanol abundances normalized to TOC, and charcoal abundances from Lake Petén Itzá core PI-NC-1. (Cont.)

Depth (cm)	Age (cal yr BP)	Date (BCE/CE)	Ti (cps)	MS (SI)	TOC (wt %)	TN (wt %)	C/N mass ratio	$\delta^{15}N_{org}$ (‰)	$\delta^{13}C_{org}$ (‰)	Total *n*-alkanes (µg/g)	Cholesterol (µg/g of OC)	Cholestanol (µg/g of OC)	Stigmastanol (µg/g of OC)	Coprostanol + Epicoprostanol (µg/g of OC)	Charcoal (particles/ cm^3)
92.5	817	1133	20094	0.23											
93	823	1127	19875		3.36	0.29	11.59	2.82	-24.85						71
93.5	829	1121	20709	0.2284											
94	835	1115	21348												61
94.5	841	1109	21638	0.226											
95	847	1103	21542												42
95.5	854	1096	21287	0.2303											
96	860	1090	20717												73
96.5	867	1083	21241	0.2277											
97	873	1077	22896												75
97.5	880	1070	23361	0.3068											
98	886	1064	23603		3.59	0.27	13.3	2.35	-23.65						102
98.5	892	1058	21185	0.3006											
99	899	1051	22272								15.37	19.89	70.18	25.47	79
99.5	905	1045	22416	0.3013											
100	912	1038	21613												82
100.5	919	1031	21138	0.3024											
101	927	1023	20764							2.72					59
101.5	934	1016	21148	0.2264											
102	941	1009	20004												69
102.5	949	1001	19017	0.2999											
103	956	994	19935		3.81	0.29	13.14	2.39	-24.04						67
103.5	964	986	19814	0.4005											
104	971	979	20547												52
104.5	979	971	18417	0.3825											
105	986	964	21198												87
105.5	994	956	21593	0.4544											
106	1003	947	22441												61
106.5	1011	939	22994	0.5272											
107	1019	931	22347												95
107.5	1027	923	21520	0.514											
108	1035	915	21082		2.68	0.22	12.18	2.54	-24.55						44
108.5	1044	906	20604	0.6038											
109	1052	898	18730												76
109.5	1060	890	20985	0.454											
110	1068	882	20862								30.35	18.70	176.76	27.34	68
110.5	1077	873	20025	0.4626											

Table S3. Titanium abundance (from x-ray fluorescence core scanning) and magnetic susceptibility (Obrist-Farner and Rice, 2019), geochemical data, total *n*-alkane abundances, fecal sterol/stanol abundances normalized to TOC, and charcoal abundances from Lake Petén Itzá core PI-NC-1. (Cont.)

Depth (cm)	Age (cal yr BP)	Date (BCE/CE)	Ti (cps)	MS (SI)	TOC (wt %)	TN (wt %)	C/N mass ratio	$\delta^{15}N_{org}$ (‰)	$\delta^{13}C_{org}$ (‰)	Total *n*-alkanes (μg/g)	Cholesterol (μg/g of OC)	Cholestanol (μg/g of OC)	Stigmastanol (μg/g of OC)	Coprostanol + Epicoprostanol (μg/g of OC)	Charcoal (particles/ cm^3)
111	1085	865	18873							2.22					99
111.5	1094	856	18933	0.3908											
112	1103	847	20107												41
112.5	1111	839	20453	0.3842											
113	1120	830	21596		3.74	0.29	12.9	2.4	-25.24						90
113.5	1129	821	20943	0.3967											
114	1137	813	20236												84
114.5	1146	804	21647	0.4822							30.14	11.81	36.51	20.15	
115	1154	796	22135												68
115.5	1163	787	21368	0.4597											
116	1171	779	21391												52
116.5	1179	771	22154	0.4656											
117	1188	762	22613												56
117.5	1196	754	22585	0.4671											
118	1204	746	22560		3.99	0.31	12.87	2.54	-25.87						59
118.5	1212	738	23379	0.4766											
119	1221	729	25763												63
119.5	1229	721	26529	0.5351											
120	1237	713	27230												21
120.5	1246	704	27933	0.6105											
121	1254	696	24360							2.73					39
121.5	1263	687	22714	0.5379											
122	1271	679	23556												54
122.5	1279	671	22495	0.626											
123	1288	662	21246		3.66	0.28	13.07	2.74	-25.58						30
123.5	1296	654	23696	0.6265											
124	1305	645	23782												39
124.5	1313	637	25611	0.7046							12.74	17.20	59.93	31.83	
125	1321	629	29829												69
125.5	1330	620	28015	0.6602											
126	1338	612	25682												32
126.5	1346	604	24968	0.7365											
127	1354	596	26263												67
127.5	1362	588	27681	0.7545											
128	1370	580	29361		2.77	0.22	12.59	3.05	-24.19						60
128.5	1378	572	28930	0.8349											
129	1386	564	28227												70

Table S3. Titanium abundance (from x-ray fluorescence core scanning) and magnetic susceptibility (Obrist-Farner and Rice, 2019), geochemical data, total *n*-alkane abundances, fecal sterol/stanol abundances normalized to TOC, and charcoal abundances from Lake Petén Itzá core PI-NC-1. (Cont.)

Depth (cm)	Age (cal yr BP)	Date (BCE/CE)	Ti (cps)	MS (SI)	TOC (wt %)	TN (wt %)	C/N mass ratio	$\delta^{15}N_{org}$ (‰)	$\delta^{13}C_{org}$ (‰)	Total *n*-alkanes (μg/g)	Cholesterol (μg/g of OC)	Cholestanol (μg/g of OC)	Stigmastanol (μg/g of OC)	Coprostanol + Epicoprostanol (μg/g of OC)	Charcoal (particles/ cm^3)
129.5	1394	556	28590	0.8572											
130	1402	548	29356												41
130.5	1410	540	29759	0.8609											
131	1418	532	33615							2.03					88
131.5	1427	523	32462	0.8577											
132	1435	515	31208												102
132.5	1443	507	27783	0.868											
133	1451	499	27455		3.37	0.27	12.48	2.95	-25.36						105
133.5	1459	491	28174	0.943											
134	1468	482	29562												75
134.5	1476	474	29359	0.8541											
135	1484	466	29638												80
135.5	1492	458	29957	0.9238											
136	1500	450	30389												132
136.5	1509	441	29697	1.0421											
137	1517	433	28592												115
137.5	1525	425	28220	1.0616											
138	1533	417	28350		2.28	0.19	12	3.2	-23.98						99
138.5	1542	408	21756	1.2045											
139	1550	400	27932								28.93	10.75	123.72	19.40	125
139.5	1558	392	31429	1.3355											
140	1566	384	33796												68
140.5	1575	375	33576	1.2636											
141	1583	367	35400							1.41					52
141.5	1592	358	32748	1.4119											
142	1600	350	28695												50
142.5	1608	342	29641	1.373											
143	1617	333	30288		2.29	0.18	12.72	3.36	-25.04						38
143.5	1625	325	29674	1.3864											
144	1634	316	29990								19.08	17.12	156.89	27.37	35
144.5	1642	308	30417	1.3082											
145	1650	300	29196												47
145.5	1659	291	27748	1.3355											
146	1667	283	27965												33
146.5	1676	274	29375	1.2601											
147	1684	266	30443												30
147.5	1693	257	33322	1.3597											

Table S3. Titanium abundance (from x-ray fluorescence core scanning) and magnetic susceptibility (Obrist-Farner and Rice, 2019), geochemical data, total *n*-alkane abundances, fecal sterol/stanol abundances normalized to TOC, and charcoal abundances from Lake Petén Itzá core PI-NC-1. (Cont.)

Depth (cm)	Age (cal yr BP)	Date (BCE/CE)	Ti (cps)	MS (SI)	TOC (wt %)	TN (wt %)	C/N mass ratio	$\delta^{15}N_{org}$ (‰)	$\delta^{13}C_{org}$ (‰)	Total *n*-alkanes (µg/g)	Cholesterol (µg/g of OC)	Cholestanol (µg/g of OC)	Stigmastanol (µg/g of OC)	Coprostanol + Epicoprostanol (µg/g of OC)	Charcoal (particles/ cm^3)
148	1701	249	34518		2.68	0.22	12.18	3.26	-25.66						33
148.5	1710	240	35494	1.3741											
149	1718	232	35741								23.85	33.18	61.28	59.77	56
149.5	1727	223	35965	1.3766											
150	1735	215	36988												46
150.5	1744	206	36675	1.3548											
151	1752	198	37055							2.10					45
151.5	1760	190	38873	1.41											
152	1769	181	40214												47
152.5	1777	173	41463	1.4577											
153	1785	165	41870		2.11	0.19	11.11	3.49	-25.16						37
153.5	1794	156	37518	1.4667											
154	1802	148	37012												33
154.5	1810	140	35516	1.5459											
155	1819	131	36661												42
155.5	1827	123	38121	1.4169											
156	1835	115	36228							1.84					44
156.5	1844	106	35289	1.4971											
157	1852	98	37134												41
157.5	1860	90	37399	1.5222											
158	1869	81	36178		2.74	0.21	13.05	3.46	-25.87						44
158.5	1877	73	35133	1.5916											
159	1885	65	35161												38
159.5	1894	56	35291	1.7313											
160	1902	48	34892							1.40					77
160.5	1910	40	34861	1.8429											
161	1918	32	35941												133
161.5	1927	23	33513	2.1086											
162	1935	15	35431												102
162.5	1943	7	36043	2.3862											
163	1951	1	37246		1.49	0.13	11.46	5.06	-24.31						127
163.5	1960	10	46347	2.5447							10.91	21.45	67.62	24.41	
164	1968	18	61198												41
164.5	1976	26	60242	2.933											
165	1984	34	60313												136
165.5	1993	43	58855	3.0226											
166	2002	52	59095							0.46					103

Table S3. Titanium abundance (from x-ray fluorescence core scanning) and magnetic susceptibility (Obrist-Farner and Rice, 2019), geochemical data, total *n*-alkane abundances, fecal sterol/stanol abundances normalized to TOC, and charcoal abundances from Lake Petén Itzá core PI-NC-1. (Cont.)

Depth (cm)	Age (cal yr BP)	Date (BCE/CE)	Ti (cps)	MS (SI)	TOC (wt %)	TN (wt %)	C/N mass ratio	$\delta^{15}N_{org}$ (‰)	$\delta^{13}C_{org}$ (‰)	Total *n*-alkanes (µg/g)	Cholesterol (µg/g of OC)	Cholestanol (µg/g of OC)	Stigmastanol (µg/g of OC)	Coprostanol + Epicoprostanol (µg/g of OC)	Charcoal (particles/ cm^3)
166.5	2010	60	56956	3.1336											
167	2019	69	55950												56
167.5	2028	78	55899	3.1032											
168	2036	86	55834		1.13	0.12	9.42	6.08	-23.15						66
168.5	2045	95	52770	3.0818							12.94	9.49	57.84	43.08	
169	2053	103	51849												24
169.5	2062	112	51917	3.1702											
170	2071	121	54676							0.55					46
170.5	2079	129	52779	3.0883											
171	2088	138	48789												41
171.5	2097	147	52198	3.0217											
172	2106	156	53062												29
172.5	2114	164	52788	2.8867											
173	2123	173	52223		1.12	0.12	9.33	6.03	-22.88						36
173.5	2132	182	51365	2.8235							16.13	10.72	133.51	37.18	
174	2140	190	50220												60
174.5	2149	199	47607	2.8061											
175	2158	208	45937												67
175.5	2166	216	48085												
176	2174	224	44446							0.46					54
176.5	2183	233	45295	2.7078											
177	2191	241	49417												38
177.5	2199	249	50588	2.7399											
178	2207	257	53548		1.16	0.12	9.67	5.91	-23.41		31.23	12.43	64.63	55.93	63
178.5	2216	266	50210	2.7855											
179	2224	274	49658												24
179.5	2232	282	50877	2.8512											
180	2240	290	51745												35
180.5	2249	299	50500	2.9236						0.52					
181	2257	307	49969												49
181.5	2265	315	48613	2.8454											
182	2273	323	49536												32
182.5	2282	332	51371	2.793											
183	2290	340	50343		1.13	0.12	9.42	5.13	-23.49		21.47	13.72	154.22	53.70	38
183.5	2298	348	50947												
184	2306	356													46
184.5	2315	365	46692												

Table S3. Titanium abundance (from x-ray fluorescence core scanning) and magnetic susceptibility (Obrist-Farner and Rice, 2019), geochemical data, total *n*-alkane abundances, fecal sterol/stanol abundances normalized to TOC, and charcoal abundances from Lake Petén Itzá core PI-NC-1. (Cont.)

Depth (cm)	Age (cal yr BP)	Date (BCE/CE)	Ti (cps)	MS (SI)	TOC (wt %)	TN (wt %)	C/N mass ratio	$\delta^{15}N_{org}$ (‰)	$\delta^{13}C_{org}$ (‰)	Total *n*-alkanes (µg/g)	Cholesterol (µg/g of OC)	Cholestanol (µg/g of OC)	Stigmastanol (µg/g of OC)	Coprostanol + Epicoprostanol (µg/g of OC)	Charcoal (particles/ cm^3)
185	2323	373	58487	2.6486											44
185.5	2331	381	54469												
186	2339	389	49232	2.8162											75
186.5	2347	397	37815												
187	2355	405	41138	2.7756						0.36					68
187.5	2363	413	37975												
188	2371	421	35815	2.7999	1.3	0.11	11.82	4.76	-23.26		24.55	144.60	24.93	15.22	52
188.5	2379	429	35893												
189	2387	437	39207	2.798											128
189.5	2395	445	35585												
190	2403	453	34052	2.7943											57
190.5	2411	461	33969							0.69					
191	2419	469	31553	2.8101											46
191.5	2427	477	31734												
192	2435	485	37321	2.811											67
192.5	2443	493	36719												
193	2451	501	37075	2.7888	1.34	0.12	11.17	4.56	-23.37		12.56	15.66	59.09	25.44	47
193.5	2459	509	37293												
194	2466	516	36248	2.8593											29
194.5	2474	524	34964												
195	2482	532	37672	2.8688											76
195.5	2491	541	37929							0.53					
196	2499	549	40460	2.9667											74
196.5	2508	558	37759												
197	2517	567	38579	2.942											25
197.5	2525	575	37241												
198	2534	584	37184	3.0575	1.45	0.12	12.08	4.71	-23.55		16.39	15.12	55.65	26.59	51
198.5	2542	592	39328												
199	2551	601	39840	3.1264											53
199.5	2560	610	38816												
200	2568	618	39258	3.2064											46
200.5	2576	626	41695							0.62					
201	2584	634	41955	3.2569											66
201.5	2592	642	41267												
202	2600	650	43083	3.2519											46
202.5	2608	658	46994								16.05	17.29	34.75	44.33	
203	2616	666	59025	3.2241	1.63	0.15	10.87	4.62	-23.31						32

Table S3. Titanium abundance (from x-ray fluorescence core scanning) and magnetic susceptibility (Obrist-Farner and Rice, 2019), geochemical data, total *n*-alkane abundances, fecal sterol/stanol abundances normalized to TOC, and charcoal abundances from Lake Petén Itzá core PI-NC-1. (Cont.)

Depth (cm)	Age (cal yr BP)	Date (BCE/CE)	Ti (cps)	MS (SI)	TOC (wt %)	TN (wt %)	C/N mass ratio	$\delta^{15}N_{org}$ (‰)	$\delta^{13}C_{org}$ (‰)	Total *n*-alkanes (µg/g)	Cholesterol (µg/g of OC)	Cholestanol (µg/g of OC)	Stigmastanol (µg/g of OC)	Coprostanol + Epicoprostanol (µg/g of OC)	Charcoal (particles/ cm^3)
203.5	2624	674	58938												
204	2632	682	58878	3.2443											95
204.5	2640	690	60547												
205	2648	698	64329	3.1674											66
205.5	2656	706	68980							1.50					
206	2664	714	77938	3.2741											86
206.5	2672	722	70072												
207	2680	730	67839	2.8889											47
207.5	2688	738	68709								36.74	37.55	85.04	73.29	
208	2696	746	67280	2.5142	2.25	0.19	11.84	4.34	-24.16						344
208.5	2705	755	66445												
209	2713	763	55024	2.1792											69
209.5	2721	771	37692												
210	2729	779	37019	1.9127											349
210.5	2737	787	38212							1.60					
211	2745	795	32627	1.7015											377
211.5	2753	803	29609												
212	2761	811	28755	1.691											349
212.5	2769	819	37723								0.00	0.00	0.00	0.00	
213	2777	827	33135	1.646	2.58	0.19	13.58	3.79	-24.26						796
213.5	2785	835	31621												
214	2793	843	30545	1.767											324
214.5	2801	851	31073												
215	2809	859	29789	2.1285											371
215.5	2816	866	27168							1.17					
216	2824	874	26109	2.8576											569
216.5	2832	882	28299												
217	2839	889	40000	3.7021											534
217.5	2847	897	36059								0.00	0.00	0.00	0.00	
218	2855	905	47803	4.0696	2.01	0.16	12.56	3.62	-24.33						1062
218.5	2862	912	46749												
219	2870	920	44795	4.1108											543
219.5	2878	928	38576												
220	2885	935	33811	2.8843											393
220.5	2892	942	34385							2.07					
221	2898	948	30124	2.0525											546
221.5	2904	954	21695												

Table S3. Titanium abundance (from x-ray fluorescence core scanning) and magnetic susceptibility (Obrist-Farner and Rice, 2019), geochemical data, total *n*-alkane abundances, fecal sterol/stanol abundances normalized to TOC, and charcoal abundances from Lake Petén Itzá core PI-NC-1. (Cont.)

Depth (cm)	Age (cal yr BP)	Date (BCE/CE)	Ti (cps)	MS (SI)	TOC (wt %)	TN (wt %)	C/N mass ratio	$\delta^{15}N_{org}$ (‰)	$\delta^{13}C_{org}$ (‰)	Total *n*-alkanes (μg/g)	Cholesterol (μg/g of OC)	Cholestanol (μg/g of OC)	Stigmastanol (μg/g of OC)	Coprostanol + Epicoprostanol (μg/g of OC)	Charcoal (particles/ cm^3)
222	2910	960	20969	1.6116							37.49	94.83	97.25	44.48	737
222.5	2916	966	20861												
223	2923	973	22491	1.4144	2.34	0.18	13	2.99	-24.74						669
223.5	2929	979	25580												
224	2935	985	24917	1.31											961
224.5	2941	991	30019												
225	2947	997	25703	1.3401											535
225.5	2953	1003	23870							1.61					
226	2959	1009	24311	1.2627											745
226.5	2965	1015	25198												
227	2972	1022	26037	1.3627											546
227.5	2978	1028	27339												
228	2984	1034	29281	1.3652	2.46	0.2	12.3	3.04	-25.06						868
228.5	2990	1040	30584												
229	2996	1046	32356	1.3444											456
229.5	3002	1052	29122												
230	3008	1058	25996	1.4013						1.92					185
230.5	3014	1064	24447												
231	3020	1070	21816	1.4051											299
231.5	3026	1076	25969												
232	3032	1082	27007	1.5088											1476
232.5	3038	1088	33081												
233	3044	1094	25725	1.4665	2.78	0.2	13.9	2.6	-25.07						257
233.5	3050	1100	24584												
234	3055	1105	25869	1.5483											381
234.5	3061	1111	27090												
235	3067	1117	30388	1.4775											382
235.5	3073	1123	29603												
236	3079	1129	19977	1.5069											407
236.5	3085	1135	24000												
237	3091	1141	25301	1.4842											171
237.5	3097	1147	25512								14.15	43.33	36.40	52.47	
238	3103	1153	23425	1.4749	2.86	0.21	13.62	2.86	-25.32						304
238.5	3109	1159	24481												
239	3115	1165	33422	1.6116											344
239.5	3121	1171	34111												
240	3126	1176	30330	1.6985											378

Table S3. Titanium abundance (from x-ray fluorescence core scanning) and magnetic susceptibility (Obrist-Farner and Rice, 2019), geochemical data, total *n*-alkane abundances, fecal sterol/stanol abundances normalized to TOC, and charcoal abundances from Lake Petén Itzá core PI-NC-1. (Cont.)

Depth (cm)	Age (cal yr BP)	Date (BCE/CE)	Ti (cps)	MS (SI)	TOC (wt %)	TN (wt %)	C/N mass ratio	$\delta^{15}N_{org}$ (‰)	$\delta^{13}C_{org}$ (‰)	Total *n*-alkanes (µg/g)	Cholesterol (µg/g of OC)	Cholestanol (µg/g of OC)	Stigmastanol (µg/g of OC)	Coprostanol + Epicoprostanol (µg/g of OC)	Charcoal (particles/ cm^3)
240.5	3133	1183	31069							2.43					
241	3139	1189	31189	1.748											258
241.5	3146	1196	30204												
242	3152	1202	30953	1.729							16.07	29.25	47.44	29.00	229
242.5	3158	1208	25360												
243	3165	1215	28357	1.8312	2.5	0.18	13.89	2.74	-25.15						305
243.5	3171	1221	27086												
244	3178	1228	26825	1.98											429
244.5	3184	1234	27950												
245	3191	1241	26865	2.0909											260
245.5	3196	1246	24942												
246	3202	1252	26491	2.1027											352
246.5	3208	1258	28327												
247	3214	1264	25039	2.0245											372
247.5	3220	1270	23450												
248	3226	1276	25465	1.9103	2.37	0.17	13.94	2.77	-24.51						359
248.5	3232	1282	26038												
249	3238	1288	30076	1.7735											394
249.5	3243	1293	30611												
250	3249	1299	25157	1.7446											328
250.5	3255	1305	25670							1.53					
251	3261	1311	24600	1.835											310
251.5	3267	1317	25572												
252	3273	1323	26843	1.9218											432
252.5	3279	1329	28000												
253	3285	1335	28428	1.9424	3.17	0.23	13.78	2.42	-25.62						483
253.5	3291	1341	32844												
254	3297	1347	23937	1.7303											421
254.5	3303	1353	22055												
255	3309	1359	20383	1.6165											346
255.5	3315	1365	22200												
256	3321	1371	24499	1.4741											469
256.5	3327	1377	24997								33.23	56.97	266.39	42.36	
257	3333	1383	26415	1.4738											349
257.5	3339	1389	28684												
258	3345	1395	30028	1.4504	1.73	0.16	10.81	2.66	-24.7						237
258.5	3352	1402	26799												

Table S3. Titanium abundance (from x-ray fluorescence core scanning) and magnetic susceptibility (Obrist-Farner and Rice, 2019), geochemical data, total *n*-alkane abundances, fecal sterol/stanol abundances normalized to TOC, and charcoal abundances from Lake Petén Itzá core PI-NC-1. (Cont.)

Depth (cm)	Age (cal yr BP)	Date (BCE/CE)	Ti (cps)	MS (SI)	TOC (wt %)	TN (wt %)	C/N mass ratio	$\delta^{15}N_{org}$ (‰)	$\delta^{13}C_{org}$ (‰)	Total *n*-alkanes (µg/g)	Cholesterol (µg/g of OC)	Cholestanol (µg/g of OC)	Stigmastanol (µg/g of OC)	Coprostanol + Epicoprostanol (µg/g of OC)	Charcoal (particles/ cm^3)
259	3358	1408	27847	1.4137											434
259.5	3364	1414	23744												
260	3370	1420	22063	1.387						1.71					356
260.5	3376	1426	20417												
261	3382	1432	21087	1.2897											320
261.5	3388	1438	24553								28.11	34.23	41.25	3.07	
262	3394	1444	24553	1.2925											356
262.5	3400	1450	24067												
263	3406	1456	29514	1.2859	2.12	0.19	11.16	2.55	-24.04						233
263.5	3412	1462	29057												
264	3418	1468	27715	1.2469											262
264.5	3423	1473	25288												
265	3429	1479	24234	1.1591											256
265.5	3435	1485	19491												
266	3441	1491	20290	1.1196											319
266.5	3446	1496	21700												
267	3452	1502	22675	1.0713							24.33	28.55	51.88	44.02	308
267.5	3457	1507	23103												
268	3463	1513	23236	1.0567	2.54	0.18	14.11	2.6	-24.86						458
268.5	3468	1518	21664												
269	3474	1524	19285	1.105											337
269.5	3479	1529	19858												
270	3485	1535	20702	1.1828											363
270.5	3491	1541	20038												
271	3496	1546	22099	1.1954						1.61					330
271.5	3502	1552	24552												
272	3508	1558	23125	1.1184											312
272.5	3513	1563	22221												
273	3519	1569	20745	1.1395	2.73	0.2	13.65	2.59	-25.31						265
273.5	3524	1574	20441												
274	3530	1580	21737	1.1332											316
274.5	3536	1586	25228												
275	3541	1591	24933	1.2205											412
275.5	3547	1597	28180												
276	3553	1603	35440	1.2231											388
276.5	3559	1609	28218												
277	3564	1614	25347	1.1302											305

Table S3. Titanium abundance (from x-ray fluorescence core scanning) and magnetic susceptibility (Obrist-Farner and Rice, 2019), geochemical data, total *n*-alkane abundances, fecal sterol/stanol abundances normalized to TOC, and charcoal abundances from Lake Petén Itzá core PI-NC-1. (Cont.)

Depth (cm)	Age (cal yr BP)	Date (BCE/CE)	Ti (cps)	MS (SI)	TOC (wt %)	TN (wt %)	C/N mass ratio	$\delta^{15}N_{org}$ (‰)	$\delta^{13}C_{org}$ (‰)	Total *n*-alkanes (µg/g)	Cholesterol (µg/g of OC)	Cholestanol (µg/g of OC)	Stigmastanol (µg/g of OC)	Coprostanol + Epicoprostanol (µg/g of OC)	Charcoal (particles/ cm^3)
277.5	3570	1620	26135												
278	3576	1626	23650	1.1314	2.6	0.19	13.68	2.51	-24.85						338
278.5	3582	1632	22003												
279	3587	1637	21708	1.0482											383
279.5	3593	1643	23847												
280	3599	1649	21013	1.0232											330
280.5	3604	1654	18304												
281	3610	1660	18550	0.9879						1.76					275
281.5	3616	1666	20518												
282	3622	1672	21155	0.9808											542
282.5	3627	1677	20215												
283	3633	1683	22895	0.9834	3.34	0.24	13.92	2.08	-25.06						395
283.5	3639	1689	23125												
284	3644	1694	25483												307
284.5	3650	1700													
285	3656	1706		1.0751											451
285.5	3661	1711	21177												
286	3667	1717	23595	1.1766											401
286.5	3673	1723	21462								26.41	46.10	34.02	40.57	
287	3678	1728	21311	1.1613											326
287.5	3684	1734	23939												
288	3689	1739	24092	1.1935	3.69	0.24	15.38	2.4	-24.64						360
288.5	3695	1745	29448												
289	3701	1751	27138	1.1884											316
289.5	3706	1756	25372												
290	3712	1762	21569	1.0831											445
290.5	3717	1767	24670												
291	3723	1773	25582	1.088											499
291.5	3729	1779	25640												
292	3734	1784	27126	1.146											440
292.5	3740	1790	28453												
293	3746	1796	28554	1.2404	3.88	0.26	14.92	2.53	-26.6						604
293.5	3751	1801	26058												
294	3757	1807	26880	1.1793											511
294.5	3763	1813	29575												
295	3768	1818	23294	1.1617											313
295.5	3774	1824	20748												

Table S3. Titanium abundance (from x-ray fluorescence core scanning) and magnetic susceptibility (Obrist-Farner and Rice, 2019), geochemical data, total *n*-alkane abundances, fecal sterol/stanol abundances normalized to TOC, and charcoal abundances from Lake Petén Itzá core PI-NC-1. (Cont.)

Depth (cm)	Age (cal yr BP)	Date (BCE/CE)	Ti (cps)	MS (SI)	TOC (wt %)	TN (wt %)	C/N mass ratio	$\delta^{15}N_{org}$ (‰)	$\delta^{13}C_{org}$ (‰)	Total *n*-alkanes (μg/g)	Cholesterol (μg/g of OC)	Cholestanol (μg/g of OC)	Stigmastanol (μg/g of OC)	Coprostanol + Epicoprostanol (μg/g of OC)	Charcoal (particles/ cm^3)
296	3780	1830	21354	1.1304											361
296.5	3786	1836	21031												
297	3791	1841	22527	1.0788											398
297.5	3797	1847	22434												
298	3803	1853	21065	0.999	3.15	0.21	15	2.29	-24.74						339
298.5	3809	1859	19732												
299	3814	1864	18235	1.0139											432
299.5	3820	1870	19525												
300	3826	1876	20640	1.0662							148.08	35.06	35.69	29.27	458
300.5	3832	1882	18286												
301	3838	1888	19821	1.093						2.68					407
301.5	3844	1894	19406												
302	3850	1900	21869	1.183											297
302.5	3857	1907	31015												
303	3863	1913	28883	1.2512	3.75	0.26	14.42	2.6	-26.44						439
303.5	3869	1919	27878												
304	3875	1925	32486	1.3057											294
304.5	3881	1931	32968												
305	3887	1937	33523	1.3043											222
305.5	3895	1945	27058												
306	3903	1953	24006	1.3029							27.93	28.15	18.01	3.10	404
306.5	3911	1961	29021												
307	3919	1969	32406	1.2876											376
307.5	3927	1977	33221												
308	3935	1985	29667	1.215	2.85	0.22	12.95	2.36	-24.44						290
308.5	3943	1993	25065												
309	3951	2001	20893	1.1545											321
309.5	3959	2009	23446												
310	3966	2016	22252	1.1955						2.06					268
310.5	3974	2024	22021												
311	3982	2032	23575	1.1082											356
311.5	3990	2040	17553								30.96	28.86	29.80	2.71	
312	3998	2048	18522	1.1134											382
312.5	4006	2056	21712												
313	4014	2064	22924	1.2184	3.74	0.27	13.85	2.22	-25.7						525
313.5	4022	2072	29362												
314	4030	2080	28130	1.2666											

Table S3. Titanium abundance (from x-ray fluorescence core scanning) and magnetic susceptibility (Obrist-Farner and Rice, 2019), geochemical data, total *n*-alkane abundances, fecal sterol/stanol abundances normalized to TOC, and charcoal abundances from Lake Petén Itzá core PI-NC-1. (Cont.)

Depth (cm)	Age (cal yr BP)	Date (BCE/CE)	Ti (cps)	MS (SI)	TOC (wt %)	TN (wt %)	C/N mass ratio	$\delta^{15}N_{org}$ (‰)	$\delta^{13}C_{org}$ (‰)	Total *n*-alkanes (μg/g)	Cholesterol (μg/g of OC)	Cholestanol (μg/g of OC)	Stigmastanol (μg/g of OC)	Coprostanol + Epicoprostanol (μg/g of OC)	Charcoal (particles/ cm^3)
314.5	4038	2088	24738												
315	4046	2096	25861	1.2567											
315.5	4054	2104	24284												
316	4062	2112	26554	1.2231											
316.5	4070	2120	28166												
317	4078	2128	26945	1.3372											
317.5	4086	2136	29623												
318	4095	2145	32522	1.3168											
318.5	4103	2153	30887												
319	4111	2161	33854	1.3625											
319.5	4119	2169	25946												
320	4127	2177	32834	1.4477											
320.5	4135	2185	28886												
321	4143	2193	26446	1.3994											
321.5	4151	2201	26842												
322	4159	2209	28066	1.3307											
322.5	4167	2217	26314												
323	4174	2224	28921	1.349											
323.5	4182	2232	27862												
324	4190	2240	26367	1.3689											
324.5	4198	2248	28484												
325	4206	2256	30189	1.3782											
325.5	4214	2264	30690												
326	4222	2272	28188	1.4369											
326.5	4230	2280	28791												
327	4238	2288	33123	1.5083											
327.5	4247	2297	35147												
328	4255	2305	37465	1.4913											
328.5	4263	2313	34324												
329	4271	2321	27589	1.4437											
329.5	4279	2329	25888												
330	4287	2337	33198	1.4458							30.43	23.39	41.58	41.14	
330.5	4295	2345	23648												
331	4303	2353	29449	1.3884											
331.5	4311	2361	37911												
332	4319	2369	26891	1.3899											
332.5	4328	2378	28979												

Table S3. Titanium abundance (from x-ray fluorescence core scanning) and magnetic susceptibility (Obrist-Farner and Rice, 2019), geochemical data, total *n*-alkane abundances, fecal sterol/stanol abundances normalized to TOC, and charcoal abundances from Lake Petén Itzá core PI-NC-1. (Cont.)

Depth (cm)	Age (cal yr BP)	Date (BCE/CE)	Ti (cps)	MS (SI)	TOC (wt %)	TN (wt %)	C/N mass ratio	$\delta^{15}N_{org}$ (‰)	$\delta^{13}C_{org}$ (‰)	Total *n*-alkanes (μg/g)	Cholesterol (μg/g of OC)	Cholestanol (μg/g of OC)	Stigmastanol (μg/g of OC)	Coprostanol + Epicoprostanol (μg/g of OC)	Charcoal (particles/ cm^3)
333	4336	2386	25604	1.2253											
333.5	4344	2394	28439												
334	4352	2402	25487	1.2372											
334.5	4360	2410	26580												
335	4368	2418	31871	1.296											
335.5	4376	2426	27796												
336	4384	2434	26166	1.3042											
336.5	4392	2442	25690												
337	4400	2450	26431	1.351											
337.5	4408	2458	30367												
338	4416	2466	39336	1.3701											
338.5	4424	2474	36024												
339	4432	2482	28973	1.3876							18.79	23.18	35.47	22.35	
339.5	4439	2489	29572												
340	4447	2497	27023	1.3719											
340.5	4455	2505	32931												
341	4463	2513	27197	1.3719											
341.5	4471	2521	30631												
342	4479	2529	26803	1.2962											
342.5	4487	2537	25673												
343	4495	2545	31752	1.2269											
343.5	4503	2553	26226												
344	4511	2561	22673	1.2011											
344.5	4519	2569	24162												
345	4527	2577	29405	1.1529											
345.5	4535	2585	34833												
346	4543	2593	27066	1.0469											
346.5	4551	2601	21399												
347	4559	2609	17536	0.9312											
347.5	4567	2617	16875												
348	4575	2625	21482	1.0038											
348.5	4583	2633	19239								11.08	13.53	29.86	15.21	
349	4591	2641	19035	1.0738											
349.5	4600	2650	20869												
350	4608	2658	21773	1.0983											
350.5	4616	2666	25936												
351	4624	2674	25782	1.259											

Table S3. Titanium abundance (from x-ray fluorescence core scanning) and magnetic susceptibility (Obrist-Farner and Rice, 2019), geochemical data, total *n*-alkane abundances, fecal sterol/stanol abundances normalized to TOC, and charcoal abundances from Lake Petén Itzá core PI-NC-1. (Cont.)

Depth (cm)	Age (cal yr BP)	Date (BCE/CE)	Ti (cps)	MS (SI)	TOC (wt %)	TN (wt %)	C/N mass ratio	$\delta^{15}N_{org}$ (‰)	$\delta^{13}C_{org}$ (‰)	Total *n*-alkanes (µg/g)	Cholesterol (µg/g of OC)	Cholestanol (µg/g of OC)	Stigmastanol (µg/g of OC)	Coprostanol + Epicoprostanol (µg/g of OC)	Charcoal (particles/ cm^3)
351.5	4632	2682	28330												
352	4640	2690	29294	1.2838											
352.5	4648	2698	26183												
353	4656	2706	26087	1.2788							21.74	22.85	37.27	41.10	
353.5	4664	2714	23319												
354	4672	2722	31134	1.3124											
354.5	4680	2730	31215												
355	4688	2738	24202	1.3408											
355.5	4696	2746	27806												
356	4704	2754	34050	1.3454											
356.5	4712	2762	26819												
357	4720	2770	26329	1.4073											
357.5	4728	2778	33450												
358	4736	2786	29334	1.337											
358.5	4744	2794	29935												
359	4752	2802	27285	1.3993											
359.5	4760	2810	27403												
360	4768	2818	28762	1.3249											
360.5	4776	2826	26784												
361	4784	2834	25988	1.3341											
361.5	4792	2842	26456												
362	4800	2850	26288	1.4901											
362.5	4809	2859	26821								17.55	16.40	32.09	25.48	
363	4817	2867	25567	1.637											
363.5	4825	2875	28714												
364	4833	2883	29004	1.8254											
364.5	4841	2891	41951												
365	4849	2899	32835	2.1496											
365.5	4857	2907	27177												
366	4866	2916	43897	2.2724											
366.5	4874	2924	45028												
367	4882	2932	39464	2.1441											
367.5	4890	2940	39420												
368	4898	2948	47640	1.8981											
368.5	4907	2957	45561												
369	4915	2965	38690	1.645											
369.5	4923	2973	37914												

Table S3. Titanium abundance (from x-ray fluorescence core scanning) and magnetic susceptibility (Obrist-Farner and Rice, 2019), geochemical data, total *n*-alkane abundances, fecal sterol/stanol abundances normalized to TOC, and charcoal abundances from Lake Petén Itzá core PI-NC-1. (Cont.)

Depth (cm)	Age (cal yr BP)	Date (BCE/CE)	Ti (cps)	MS (SI)	TOC (wt %)	TN (wt %)	C/N mass ratio	$\delta^{15}N_{org}$ (‰)	$\delta^{13}C_{org}$ (‰)	Total *n*-alkanes (µg/g)	Cholesterol (µg/g of OC)	Cholestanol (µg/g of OC)	Stigmastanol (µg/g of OC)	Coprostanol + Epicoprostanol (µg/g of OC)	Charcoal (particles/ cm^3)
370	4931	2981	36904	1.5426											
370.5	4939	2989	32342												
371	4948	2998	31429	1.4474											
371.5	4956	3006	27273								39.48	22.29	21.83	6.31	
372	4964	3014	22587	1.5389											
372.5	4972	3022	21167												
373	4980	3030	23646	1.6841											
373.5	4988	3038	23910												
374	4996	3046	26356	1.7242											
374.5	5004	3054	28331												
375	5012	3062	29508	1.814											
375.5	5020	3070	30355												
376	5028	3078	29641	1.8437											
376.5	5036	3086	30031												
377	5043	3093	30165	1.7199											
377.5	5051	3101	26051												
378	5059	3109	33054	1.7028											
378.5	5067	3117	31585												
379	5075	3125	30398	1.5252											
379.5	5083	3133	31059												
380	5091	3141	31352	1.429											
380.5	5099	3149	28140								22.07	18.86	39.99	41.30	
381	5107	3157	24772	1.4335											
381.5	5115	3165	24149												
382	5123	3173	21189	1.3612											
382.5	5131	3181	25425												
383	5139	3189	22653	1.4312											
383.5	5147	3197	25938												
384	5155	3205	28359												
384.5	5163	3213		1.6079											
385	5172	3222													
385.5	5180	3230	23544	1.6578											
386	5188	3238	24394												
386.5	5196	3246	25693	1.7328											
387	5205	3255	28455												
387.5	5213	3263	28787	1.8032											
388	5221	3271	31355												

Table S3. Titanium abundance (from x-ray fluorescence core scanning) and magnetic susceptibility (Obrist-Farner and Rice, 2019), geochemical data, total *n*-alkane abundances, fecal sterol/stanol abundances normalized to TOC, and charcoal abundances from Lake Petén Itzá core PI-NC-1. (Cont.)

Depth (cm)	Age (cal yr BP)	Date (BCE/CE)	Ti (cps)	MS (SI)	TOC (wt %)	TN (wt %)	C/N mass ratio	$\delta^{15}N_{org}$ (‰)	$\delta^{13}C_{org}$ (‰)	Total *n*-alkanes (μg/g)	Cholesterol (μg/g of OC)	Cholestanol (μg/g of OC)	Stigmastanol (μg/g of OC)	Coprostanol + Epicoprostanol (μg/g of OC)	Charcoal (particles/ cm^3)
388.5	5229	3279	31398	1.9239											
389	5238	3288	40991												
389.5	5246	3296	45552	1.7446											
390	5254	3304	41778								18.90	18.05	89.24	37.68	
390.5	5262	3312	27554	1.6499											
391	5270	3320	22722												
391.5	5278	3328	21785	1.6478											
392	5285	3335	26827												
392.5	5293	3343	25412	1.7773											
393	5301	3351	28263												
393.5	5309	3359	35601	1.835											
394	5317	3367	33293												
394.5	5324	3374	32640	1.82							23.00	25.64	37.78	49.73	
395	5332	3382	37296												
395.5	5340	3390	35848	1.8132											
396	5348	3398	37232												
396.5	5357	3407	42253	1.8076											
397	5365	3415	36784												
397.5	5373	3423	31700	1.7403											
398	5381	3431	30351												
398.5	5389	3439	27744	1.7773											
399	5397	3447	33505												
399.5	5406	3456	35800	1.7962											
400	5414	3464	32576												
400.5	5422	3472	33326	1.774											
401	5430	3480	41654												
401.5	5438	3488	41906	1.7442											
402	5446	3496	39295												
402.5	5455	3505	41404	1.6376											
403	5463	3513	42370												
403.5	5471	3521	28912	1.6545											
404	5479	3529	21673												
404.5	5487	3537	25807	1.6255											
405	5495	3545	29828												
405.5	5503	3553	35495	1.6338											
406	5511	3561	34259												
406.5	5519	3569	36254	1.6932											

Table S3. Titanium abundance (from x-ray fluorescence core scanning) and magnetic susceptibility (Obrist-Farner and Rice, 2019), geochemical data, total *n*-alkane abundances, fecal sterol/stanol abundances normalized to TOC, and charcoal abundances from Lake Petén Itzá core PI-NC-1. (Cont.)

Depth (cm)	Age (cal yr BP)	Date (BCE/CE)	Ti (cps)	MS (SI)	TOC (wt %)	TN (wt %)	C/N mass ratio	$\delta^{15}N_{org}$ (‰)	$\delta^{13}C_{org}$ (‰)	Total *n*-alkanes (µg/g)	Cholesterol (µg/g of OC)	Cholestanol (µg/g of OC)	Stigmastanol (µg/g of OC)	Coprostanol + Epicoprostanol (µg/g of OC)	Charcoal (particles/ cm^3)
407	5528	3578	31336												
407.5	5536	3586	28657	1.6043											
408	5544	3594	36001												
408.5	5552	3602	35959	1.4618							17.40	24.17	13.60	2.36	
409	5560	3610	30172												
409.5	5568	3618	30864	1.4413											
410	5576	3626	24330												
410.5	5584	3634	20198	1.4998											
411	5592	3642	21044												
411.5	5601	3651	26175	1.4987											
412	5609	3659	31489												
412.5	5617	3667	41144	1.4211											
413	5625	3675	29149												
413.5	5634	3684		1.4165											
414	5642	3692	20625												
414.5	5650	3700	21379	1.4296											
415	5658	3708	22380												
415.5	5666	3716	25082	1.3505											
416	5674	3724	25706												
416.5	5682	3732	25107	1.4301											
417	5690	3740	21279												
417.5	5698	3748	23055	1.5053											
418	5706	3756	29462								20.48	20.38	50.01	35.39	
418.5	5714	3764	39619	1.4906											
419	5722	3772	28370												
419.5	5730	3780	28223	1.4691											
420	5738	3788	35273												
420.5	5746	3796	27010	1.6014											
421	5754	3804	22828												
421.5	5762	3812	21060	1.6496											
422	5770	3820	21509												
422.5	5778	3828	24534	1.6594							45.84	24.15	37.45	38.32	
423	5786	3836	25358												
423.5	5794	3844	25598	1.6632											
424	5802	3852	28732												
424.5	5810	3860	30987	1.7921											
425	5817	3867	29730												

Table S3. Titanium abundance (from x-ray fluorescence core scanning) and magnetic susceptibility (Obrist-Farner and Rice, 2019), geochemical data, total *n*-alkane abundances, fecal sterol/stanol abundances normalized to TOC, and charcoal abundances from Lake Petén Itzá core PI-NC-1. (Cont.)

Depth (cm)	Age (cal yr BP)	Date (BCE/CE)	Ti (cps)	MS (SI)	TOC (wt %)	TN (wt %)	C/N mass ratio	$\delta^{15}N_{org}$ (‰)	$\delta^{13}C_{org}$ (‰)	Total *n*-alkanes (µg/g)	Cholesterol (µg/g of OC)	Cholestanol (µg/g of OC)	Stigmastanol (µg/g of OC)	Coprostanol + Epicoprostanol (µg/g of OC)	Charcoal (particles/ cm^3)
425.5	5825	3875	27432	1.8283											
426	5833	3883	32042												
426.5	5841	3891	30395	1.9217											
427	5849	3899	28241												
427.5	5857	3907	37873	1.8327											
428	5865	3915	31295												
428.5	5873	3923	34466	1.6805											
429	5881	3931	31381												
429.5	5889	3939	28442	1.7009											
430	5897	3947	25817												
430.5	5905	3955	28711	1.5609											
431	5913	3963	26267												
431.5	5921	3971	24751	1.5119											
432	5929	3979	22350												
432.5	5937	3987	21400	1.5368											
433	5945	3995	24081												
433.5	5953	4003	32199	1.5348											
434	5961	4011	29196												
434.5	5969	4019	29821	1.714											
435	5977	4027	22448												
435.5	5985	4035	27918	1.7336											
436	5993	4043	34470												
436.5	6001	4051	31536	1.6724											
437	6009	4059	35580												
437.5	6017	4067	32926	1.6769											
438	6025	4075	23846												
438.5	6033	4083	23553	1.5995											
439	6041	4091	26053												
439.5	6049	4099	27765	1.6905											
440	6057	4107	26183												
440.5	6065	4115	28137	1.7446											
441	6073	4123	30078												
441.5	6080	4130	31435	1.781							21.96	19.72	34.38	21.44	
442	6088	4138	31237												
442.5	6096	4146	29141	1.8437											
443	6104	4154	30872												
443.5	6112	4162	33829	2.0202											

Table S3. Titanium abundance (from x-ray fluorescence core scanning) and magnetic susceptibility (Obrist-Farner and Rice, 2019), geochemical data, total *n*-alkane abundances, fecal sterol/stanol abundances normalized to TOC, and charcoal abundances from Lake Petén Itzá core PI-NC-1. (Cont.)

Depth (cm)	Age (cal yr BP)	Date (BCE/CE)	Ti (cps)	MS (SI)	TOC (wt %)	TN (wt %)	C/N mass ratio	$\delta^{15}N_{org}$ (‰)	$\delta^{13}C_{org}$ (‰)	Total *n*-alkanes (µg/g)	Cholesterol (µg/g of OC)	Cholestanol (µg/g of OC)	Stigmastanol (µg/g of OC)	Coprostanol + Epicoprostanol (µg/g of OC)	Charcoal (particles/ cm^3)
444	6120	4170	26226												
444.5	6128	4178	29074												
445	6136	4186	38097												
445.5	6144	4194	42391	2.2958											
446	6152	4202	36661												
446.5	6160	4210	37785	2.2794											
447	6168	4218	43552												
447.5	6176	4226	44566	2.1915											
448	6184	4234	47461												
448.5	6192	4242	36782	2.0727											
449	6200	4250	35135												
449.5	6208	4258	32386	1.9197											
450	6216	4266	29225												
450.5	6224	4274	32048	1.9225											
451	6232	4282	27628												
451.5	6240	4290	27152	1.8166											
452	6248	4298	28346												
452.5	6256	4306	26678	1.6517											
453	6264	4314	26706												
453.5	6272	4322	23902	1.5605											
454	6280	4330	23312												
454.5	6288	4338	23478	1.5084											
455	6297	4347	23734												
455.5	6305	4355	26937	1.7307											
456	6313	4363	27315												
456.5	6321	4371	29623	1.7744											
457	6329	4379	29731												
457.5	6337	4387	29703	1.8872											
458	6345	4395	27602												
458.5	6353	4403	27851	2.0168											
459	6361	4411	25442												
459.5	6369	4419	25301	2.1173											
460	6377	4427	26217								17.88	18.74	34.99	32.81	
460.5	6385	4435	28816	2.0865											
461	6393	4443	30265												
461.5	6401	4451	33912	2.088											
462	6408	4458	36793												

Table S3. Titanium abundance (from x-ray fluorescence core scanning) and magnetic susceptibility (Obrist-Farner and Rice, 2019), geochemical data, total *n*-alkane abundances, fecal sterol/stanol abundances normalized to TOC, and charcoal abundances from Lake Petén Itzá core PI-NC-1. (Cont.)

Depth (cm)	Age (cal yr BP)	Date (BCE/CE)	Ti (cps)	MS (SI)	TOC (wt %)	TN (wt %)	C/N mass ratio	$\delta^{15}N_{org}$ (‰)	$\delta^{13}C_{org}$ (‰)	Total *n*-alkanes (μg/g)	Cholesterol (μg/g of OC)	Cholestanol (μg/g of OC)	Stigmastanol (μg/g of OC)	Coprostanol + Epicoprostanol (μg/g of OC)	Charcoal (particles/ cm^3)
462.5	6416	4466	33433	2.1392											
463	6424	4474	32195												
463.5	6432	4482	29707	2.0065											
464	6440	4490	33551												
464.5	6448	4498	30507	1.941											
465	6456	4506	26665								20.72	24.75	52.29	37.62	
465.5	6463	4513	27324	1.7415											
466	6471	4521	29269												
466.5	6479	4529	28958	1.775											
467	6487	4537	30811												
467.5	6495	4545	22844	1.7376											
468	6502	4552	19572												
468.5	6510	4560	21172	1.6787											
469	6518	4568	23063												
469.5	6526	4576	23643	1.6517											
470	6533	4583	23195												
470.5	6542	4592	25925	1.7313											
471	6550	4600	29639												
471.5	6558	4608	32688	1.7409											
472	6566	4616	33359												
472.5	6574	4624	35083	1.7803											
473	6582	4632	34674												
473.5	6591	4641	29626	1.7524											
474	6599	4649	27648												
474.5	6607	4657	27485	1.7703											
475	6615	4665	26732												
475.5	6623	4673	29603	1.8182											
476	6631	4681	34189												
476.5	6639	4689	30205	1.8437											
477	6646	4696	26987												
477.5	6654	4704	31356	1.9536											
478	6662	4712	26802												
478.5	6670	4720	22253	1.999											
479	6677	4727	28511								1.86	0.00	0.00	0.00	
479.5	6685	4735	32704	2.1118											
480	6693	4743	35982												
480.5	6701	4751	40381	2.0681											

Table S3. Titanium abundance (from x-ray fluorescence core scanning) and magnetic susceptibility (Obrist-Farner and Rice, 2019), geochemical data, total *n*-alkane abundances, fecal sterol/stanol abundances normalized to TOC, and charcoal abundances from Lake Petén Itzá core PI-NC-1. (Cont.)

Depth (cm)	Age (cal yr BP)	Date (BCE/CE)	Ti (cps)	MS (SI)	TOC (wt %)	TN (wt %)	C/N mass ratio	$\delta^{15}N_{org}$ (‰)	$\delta^{13}C_{org}$ (‰)	Total *n*-alkanes (µg/g)	Cholesterol (µg/g of OC)	Cholestanol (µg/g of OC)	Stigmastanol (µg/g of OC)	Coprostanol + Epicoprostanol (µg/g of OC)	Charcoal (particles/ cm^3)
481	6708	4758	37528												
481.5	6716	4766	36836	2.0225											
482	6724	4774	40391												
482.5	6732	4782	33271	2.0113											
483	6739	4789	36814												
483.5	6747	4797	36883	2.0015							19.94	23.66	73.74	49.49	
484	6755	4805	34817												
484.5	6762	4812	35735	1.9352											
485	6770	4820	38071												
485.5	6777	4827	31208	1.7861											
486	6785	4835	35900												
486.5	6792	4842	32200	1.7904											
487	6799	4849	30800												
487.5	6806	4856	31216	1.7515											
488	6813	4863	26606												
488.5	6820	4870	29186	1.7881											
489	6828	4878	32288												
489.5	6835	4885	41234	1.8481											
490	6842	4892	44555												
490.5	6847	4897	35003	1.9334											
491	6852	4902	35519												
491.5	6857	4907	36490	1.9134											
492	6862	4912	31435												
492.5	6867	4917	43286	1.9765											
493	6872	4922	42092												
493.5	6877	4927	30033	1.9864							19.24	31.31	30.00	4.25	
494	6881	4931	38083												
494.5	6886	4936	35347	1.9817											
495	6891	4941	34750												
495.5	6896	4946	30752	1.8714											
496	6901	4951	31699												
496.5	6906	4956	35769	1.9835											
497	6911	4961	30407												
497.5	6916	4966	36066	1.9835											
498	6921	4971	41489												
498.5	6926	4976	36973	1.952											
499	6931	4981	41740												

Table S3. Titanium abundance (from x-ray fluorescence core scanning) and magnetic susceptibility (Obrist-Farner and Rice, 2019), geochemical data, total *n*-alkane abundances, fecal sterol/stanol abundances normalized to TOC, and charcoal abundances from Lake Petén Itzá core PI-NC-1. (Cont.)

Depth (cm)	Age (cal yr BP)	Date (BCE/CE)	Ti (cps)	MS (SI)	TOC (wt %)	TN (wt %)	C/N mass ratio	$\delta^{15}N_{org}$ (‰)	$\delta^{13}C_{org}$ (‰)	Total *n*-alkanes (μg/g)	Cholesterol (μg/g of OC)	Cholestanol (μg/g of OC)	Stigmastanol (μg/g of OC)	Coprostanol + Epicoprostanol (μg/g of OC)	Charcoal (particles/ cm^3)
499.5	6936	4986	34777	1.8688											
500	6941	4991	32638								25.39	28.19	34.48	30.11	
500.5	6946	4996	34677	1.8691											
501	6951	5001	32835												
501.5	6956	5006	32154	1.9315											
502	6961	5011	32350												
502.5	6967	5017	36745	1.9159											
503	6972	5022	47912												
503.5	6977	5027	34583	1.8858											
504	6982	5032	28021												
504.5	6987	5037	36352	1.9813											
505	6992	5042	34860												
505.5	6997	5047	35232	2.0671											
506	7002	5052	43819												
506.5	7007	5057	39242	2.073											
507	7012	5062	35344												
507.5	7017	5067	35791	2.0451							32.76	36.61	76.70	50.79	
508	7021	5071	51263												
508.5	7026	5076	48075	1.9396											
509	7031	5081	47002												
509.5	7036	5086	40377	2.0057											
510	7041	5091	41119												
510.5	7046	5096	49260	1.9761											
511	7051	5101	60551												
511.5	7056	5106	59377	1.7256											
512	7061	5111	56644												
512.5	7066	5116	39470	1.428											
513	7071	5121	42697												
513.5	7076	5126	34949	1.2039											
514	7081	5131	19459												
514.5	7086	5136	18483												
515	7091	5141	18593								33.04	38.38	27.02	5.67	

REFERENCES

Anselmetti, F.S., Ariztegui, D., Hodell, D.A., Hillesheim, M.B., Brenner, M., Gili, A., McKenzie, J.A., & Mueller, A.D. (2006). Late Quaternary climate-induced lake level variations in Lake Petén Itzá, Guatemala, inferred from seismic stratigraphic analysis. *Palaeogeogr. Palaeoclimatol. Palaeoecol., 230*, 52–69. doi:10.1016/j.palaeo.2005.06.037

Anselmetti, F.S., Hodell, D.A., Ariztegui, D., Brenner, M., & Rosenmeier, M.F. (2007). Quantification of soil erosion rates related to ancient Maya deforestation. *Geology, 35*(10), 915–918. doi: 10.1130/G23834A.1

Battistel, D., Roman, M., Marchetti, A., Kehrwald, N.M., Radaelli, M., Balliana, E., Toscano, G., & Barbante, C. (2018). Anthropogenic impact in the Maya Lowlands of Petén, Guatemala, during the last 5500 years. *J. Quat. Sci.*, *33*(2), 166–176. doi: 10.1002/jqs.3013

Beach T., Luzzadder-Beach, S., Cook, D., Dunning, N., Kennett, D.J., Krause, S., Terry, R., Trein, D., & Valdez, F. (2015). Ancient Maya impacts on the Earth's surface: An Early Anthropocene analog? *Quat. Sci. Rev.*, *124*, 1–30. doi:10.1016/j.quascirev.2015.05.028

Beach T., Luzzadder-Beach, S., Krause, S., Guderjan, T., Valdez Jr., F., Fernandez-Diaz, J.C., Eshleman, S., & Doyle, C. (2019). Ancient Maya wetland fields revealed under tropical forest canopy from laser scanning and multiproxy evidence. *Proc. Natl. Acad. Sci. U.S.A.*, *116*(43), 21469–21477. doi:10.1073/pnas.1910553116

Berke, M.A. (2018). Reconstructing Terrestrial Paleoenvironments Using Sedimentary Organic Biomarkers. In D.A. Croft, D.F. Su, & S.W. Simpson (Eds.), *Methods in Paleoecology: Reconstructing Cenozoic Terrestrial Environments and Ecological Communities* (pp. 121–149). Springer, Cham. doi:10.1007/978-3-319-94265-0_8

Binford, M.W., Brenner, M., Whitmore, T.J., Higuera-Gundy, A., Deevey, E.S., & Leyden, B. (1987). Ecosystems, paleoecology and human disturbance in subtropical and tropical America. *Quat. Sci. Rev., 6*, 115–128.

Blaauw, M., & Christen, J.A. (2011). Flexible Paleoclimate Age-Depth Models Using an Autoregressive Gamma Process. *Bayesian Anal.*, *6*(3), 457–474. doi:10.1214/11-BA618

Brenner, M. (2018). The Lake Petén Itzá Watershed: Modern and Historical Ecology. In P.M. Rice & D.S. Rice (Eds.), *Historical and Archaeological Perspectives on the Itzas of Petén, Guatemala* (pp. 57–66). Boulder, CO: University Press of Colorado.

Brenner, M., Rosenmeier, M.F., Hodell, D.A., & Curtis, J.H. (2002). Paleolimnology of the Maya Lowlands: Long-term perspectives on interactions among climate, environment, and humans. *Ancient Mesoamerica, 13*, 141–157. doi:10.1017.S0956536102131063

Bull, I.D., Lockheart, M.J., Elhmmali, M.M., Roberts, D.J., & Evershed, R.P. (2002). The origin of faeces by means of biomarker detection. *Environ. Int., 27*, 647–654.

Cranwell, P.A., Eglinton, G., & Robinson, N. (1987). Lipids of aquatic organisms as potential contributors to lacustrine sediments—II. *Org. Geochem., 11*(6), 513–527.

Curtis, J.H., Brenner, M., Hodell, D.A., Balser, R.A., Islebe, G.A., & Hooghiemstra, H. (1998). A multi-proxy study of Holocene environmental change in the Maya Lowlands of Peten, Guatemala. *Journal of Paleolimnology, 19*, 139–159.

Deevey, E.S. (1985). Stress, Strain, and Stability of Lacustrine Ecosystems. In E.Y. Haworth & J.W.G. Lund (Eds.), *Lake Sediments and Environmental History* (pp. 203–229). Minneapolis, MN: University of Minnesota Press.

Deevey, E.S., Rice, D.S., Rice, P.M., Vaughan, H.H., Brenner, M., & Flannery, M.S. (1979). Maya Urbanism: Impact on a Tropical Karst Environment. *Science, 206*, 298–306.

Dunning, N.P., Beach, T.P., & Luzzadder-Beach, S. (2012). Kax and kol: Collapse and resilience in lowland Maya civilization. *Proc. Natl. Acad. Sci. U.S.A., 109*(10), 3652–3657. doi:10.1073/pnas.1114838109

Enters, D., Lücke, A., & Zolitschka, B. (2006). Effects of land-use change on deposition and composition of organic matter in Frickenhauser See, northern Bavaria, Germany. *Sci. Total Environ., 369*, 178–187. doi:10.1016/j.scitotenv.2006.05.020

Fan, J., Xiao, J., Wen, R., Zhang, S., Wang, X., Cui, L., & Yamagata, H. (2017). Carbon and nitrogen signatures of sedimentary organic matter from Dali Lake in Inner Mongolia: Implications for Holocene hydrological and ecological variations in the East Asian summer monsoon margin. *Quat. Int., 452*, 65–78. doi:10.1016/j.quaint.2016.09.050

Fellerhoff, C., Voss, M., & Wantzen, K.M. (2003). Stable carbon and nitrogen isotope signatures of decomposing tropical macrophytes. *Aquatic Ecology, 37*, 361–375. doi:10.1023/B:AECO.0000007049.25535.12

Ficken, K.J., Li, B., Swain, D.L., & Eglinton, G. (2000). An *n*-alkane proxy for the sedimentary input of submerged/floating freshwater aquatic macrophytes. *Org. Geochem., 31*, 745–749.

Fischer, E., Oldfield, F., Wake, R., Boyle, J., Appleby, P., & Wolff, G.A. (2003). Molecular marker records of land use change. *Org. Geochem., 34*, 105–119.

Fisher, M.M., Brenner, M., & Reddy, K.R. (1992). A simple, inexpensive piston corer for collecting undisturbed sediment/water interface profiles. *Journal of Paleolimnology, 7*, 157–161.

Hodell, D., Anselmetti, F., Brenner, M., Ariztegui, D., & the PISDP Scientific Party (2006). The Lake Petén Itzá Scientific Drilling Project. *Scientific Drilling, 3*, 25–29. doi:10.2204/iodp.sd.3.02.2006

Hodell, D.A., Quinn, R.L., Brenner, M., & Kamenov, G. (2004). Spatial variation of strontium isotopes ($^{87}Sr/^{86}Sr$) in the Maya region: a tool for tracking ancient human migration. *J. Archaeol. Sci., 31*, 585–601. doi:10.1016/j.jas.2003.10.009

Hollander, D.J., & McKenzie, J.A. (1991). CO_2 control on carbon-isotope fractionation during aqueous photosynthesis: A paleo-pCO_2 barometer. *Geology, 19*, 929–932.

Huang, Y., Street-Perrott, F.A., Metcalfe, S.E., Brenner, M., Moreland, M., & Freeman, K.H. (2001). Climate Change as the Dominant Control on Glacial-Interglacial Variations in C_3 and C_4 Plant Abundance. *Science, 293*, 1647–1651.

Inglett, P.W., & Reddy, K.R. (2006). Investigating the use of macrophyte stable C and N isotopic ratios as indicators of wetland eutrophication: Patterns in the P-affected Everglades. *Limnol. Oceanogr., 51*(5), 2380–2387.

Islebe, G.A., Hooghiemstra, H., Brenner, M., Curtis, J.H., & Hodell, D.A. (1996). A Holocene vegetation history from lowland Guatemala. *Holocene, 6*(3), 265–271.

Jones, G.D. (1998). *The Conquest of the Last Maya Kingdom*. Stanford, CA: Stanford University Press.

Keenan, B., Imfeld, A., Johnston, K., Breckenridge, A., Gélinas, Y., & Douglas, P.M.J. (2021). Molecular evidence for human population change associated with climate events in the Maya lowlands. *Quat. Sci. Rev., 258*, 106904. doi:10.1016/j.quascirev.2021.106904

Krause, S., Beach, T.P., Luzzadder-Beach, S., Cook, D., Bozarth, S.R., Valdez Jr., F., & Guderjan, T.H. (2021). Tropical wetland persistence through the Anthropocene: Multiproxy reconstruction of environmental change in a Maya agroecosystem. *Anthropocene, 34*, 100284. doi:10.1016/j.ancene.2021.100284

LeBlanc, L.A., Latimer, J.S., Ellis, J.T., & Quinn, J.G. (1992). The geochemistry of coprostanol in waters and surface sediments from Narragansett Bay. *Estuar. Coast. Shelf Sci., 34*, 439–458.

Leyden, B.W., Brenner, M., & Dahlin, B.H. (1998). Cultural and Climatic History of Cobá, a Lowland Maya City in Quintana Roo, Mexico. *Quat. Res., 49*, 111–122.

Lou, Y., Xu, M., Chen, X., He, X., & Zhao, K. (2012). Stratification of soil organic C, N and C:N ratio as affected by conservation tillage in two maize fields of China. *Catena*, *95,* 124–130. doi:10.1016/j.catena.2012.02.009

Mays, J.L., Brenner, M., Curtis, J.H., Curtis, K.V., Hodell, D.A., Correa-Metrio, A., Escobar, J., Dutton, A.L., Zimmerman, A.R., & Guilderson, T.P. (2017). Stable carbon isotopes ($\delta^{13}C$) of total organic carbon and long-chain *n*-alkanes as proxies for climate and environmental change in a sediment core from Lake Petén-Itzá, Guatemala. *Journal of Paleolimnology, 57,* 307–319. doi:10.1007/s10933-017-9949-z

Meyers, P.A., & Teranes, J.L. (2001). Sediment organic matter. In W.M. Last & J.P. Smol (Eds.), *Tracking Environmental Change Using Lake Sediments. Volume 2: Physical and Geochemical Methods* (pp. 239–269). Dordrecht, The Netherlands: Kluwer Academic Publishers.

Mueller A.D., Islebe, G.A., Anselmetti, F.S., Ariztegui, D., Brenner, M., Hodell, D.A., Hajdas, I., Hamann, Y., Haug, G.H., & Kennett, D.J. (2010). Recovery of the forest ecosystem in the tropical lowlands of northern Guatemala after disintegration of Classic Maya polities. *Geology, 38*(6), 523–526. doi:10.1130/G30797.1

Mueller A.D., Islebe, G.A., Hillesheim, M.B., Grzesik, D.A., Anselmetti, F.S., Ariztegui, D., Brenner, M., Curtis, J.H., Hodell, D.A., & Venz, K.A. (2009). Climate drying and associated forest decline in the lowlands of northern Guatemala during the late Holocene. *Quat. Res., 71*, 133–141. doi:10.1016/j.yqres.2008.10.002

Obrist-Farner, J., & Rice, P.M. (2019). Nixtun-Ch'ich' and its environmental impact: Sedimentological and archaeological correlates in a core from Lake Petén Itzá in the southern Maya lowlands, Guatemala. *J. Archaeol. Sci. Rep., 26,* 101868. doi:10.1016/j.jasrep.2019.05.033

Pérez L., Bugja, R., Massaferro, J., Steeb, P., van Geldern, R., Frenzel, P., Brenner, M., Scharf, B., & Schwalb, A. (2010). Post-Columbian environmental history of Lago Petén Itzá, Guatemala. *Revista Mexicana de Ciencias Geológicas, 27*(3), 490–507.

Prost, K., Birk, J.J., Lehndorff, E., Gerlach, R., & Amelung, W. (2017). Steroid Biomarkers Revisited – Improved Source Identification of Faecal Remains in Archaeological Soil Material. *PLoS One, 12*(1), e0164882. doi:10.1371/journal.pone.0164882

Pugh, T.W. (2019). From the Streets: Public and Private Space in an Early Maya City. *J. Archaeol. Method Theory, 26*, 967–997. doi:10.1007/s10816-018-9404-0

Pugh, T.W., & Rice, P.M. (2017). Early Urban Planning, Spatial Strategies, and the Maya Gridded City of Nixtun-Ch'ich', Petén, Guatemala. *Curr. Anthropol., 58*(5), 576–603. doi: 10.1086/693779

Pugh, T.W., Rice, P.M., Chan Nieto, E.M., Meranda, M.L., & Milley, D.S. (in press). Middle Preclassic hydraulic planning at Nixtun-Ch'ich', Petén, Guatemala. *Ancient Mesoamerica*.

Pugh, T.W., Rice, P.M., Chan Nieto, E., & Rice, D.S. (2016). A Chak'an Itza Center at Nixtun-Ch'ich', Petén, Guatemala. *J. Field Archaeol., 41*(1), 1–16. doi:10.1080/00934690.2015.1129253

Reimer, P.J., Austin, W.E.N., Bard, E., Bayliss, A., Blackwell, P.G., Bronk Ramsey, C., Butzin, M., Cheng, H., Lawrence Edwards, R., Friedrich, M., Grootes, P.M., Guilderson, T.P., Hajdas, I., Heaton, T.J., Hogg, A.G., Hughen, K.A., Kromer, B., Manning, S.W., Muscheler, R., Palmer, J.G., Pearson, C., van der Plicht, J., Reimer, R.W., Richards, D.A., Marian Scott, E., Southon, J.R., Turney, C.S.M., Wacker, L., Adolphi, F., Büntgen, U., Capano, M., Fahrni, S.M., Fogtmann-Schulz, A., Friedrich, R., Köhler, P., Kudsk, S., Miyake, F., Olsen, J., Reinig, F., Sakamoto, M., Sookdeo, A., & Talamo, S. (2020). The IntCal20 Northern Hemisphere Radiocarbon Age Calibration Curve (0–55 cal kBP). *Radiocarbon, 62*(4), 725–757. doi:10.1017/RDC.2020.41

Rice, P.M. (2009). Mound ZZI, Nixtun-Ch'ich', Petén, Guatemala: Rescue Operations at a Long-Lived Structure in the Maya Lowlands. *J. Field Archaeol., 34*(4), 403–422.

Rice, P.M. (2018). Wanna bet? Classic Ballcourt 2 at Nixtun-Ch'ich', Peten, Guatemala. *Latin American Antiquity, 29*(3), 610–615. doi:10.1017/laq.2018.30

Rice, P.M. (2019). Early Pottery and Construction at Nixtun-Ch'ich', Petén, Guatemala: Preliminary Observations. *Latin American Antiquity, 30*(3), 471–489. doi:10.1017/laq.2019.26

Rice, P.M., & Pugh, T.W. (2017). Water, centering, and the beginning of time at Middle Preclassic Nixtun-Ch'ich', Petén, Guatemala. *J. Anthropol. Archaeol., 48*, 1–16. doi:10.1016/j.jaa.2017.05.004

Rice, P.M., & Pugh, T.W. (2021). Middle Preclassic Nixtun-Ch'ich': A lowland Maya primate/ritual city. *J. Anthropol. Archaeol.*, *63*, 101308. doi:10.1016/j.jaa.2021.101308

Rice, P.M., Rice, D.S., & Pugh, T.W. (2017). Small Things Forgotten: Artifacts of Fishing in the Petén Lakes Region, Guatemala. In M. Quinlan & J. Nolan (Eds.), *Contributions in Ethnobiology*. Tacoma, WA: Society of Ethnobiology.

Rosenmeier, M.F., Brenner, M., Kenney, W.F., Whitmore, T.J., & Taylor C.M. (2004). Recent eutrophication in the Southern Basin of Lake Petén Itzá, Guatemala: human impact on a large tropical lake. *Hydrobiologia, 511*, 161–172.

Rosenmeier, M.F., Hodell, D.A., Brenner, M., & Curtis, J.H. (2002). A 4000-Year Lacustrine Record of Environmental Change in the Southern Maya Lowlands, Petén, Guatemala. *Quat. Res., 57*, 183–190. doi:10.1006/qres.2001.2305

Schüpbach, S., Kirchgeorg, T., Colombaroli, D., Beffa, G., Radaelli, M., Kehrwald, N.M., & Barbante, C. (2015). Combining charcoal sediment and molecular markers to infer a Holocene fire history in the Maya Lowlands of Petén, Guatemala. *Quat. Sci. Rev., 115*, 123–131. doi:10.1016/j.quascirev.2015.03.004

Sharpe, A.E., Emery, K.F., Inomata, T., Triadan, D., Kamenov, G.D., & Krigbaum, J. (2018). Earliest isotopic evidence in the Maya region for animal management and long-distance trade at the site of Ceibal, Guatemala. *Proc. Natl. Acad. Sci. U.S.A., 115*(14), 3605–3610. doi:10.1073/pnas.1713880115

Talbot, M.R. (2001). Nitrogen isotopes in palaeolimnology. In W.M. Last & J.P. Smol (Eds.), *Tracking Environmental Change Using Lake Sediments. Volume 2: Physical and Geochemical Methods* (pp. 401–439). Dordrecht, The Netherlands: Kluwer Academic Publishers.

Thienemann, M., Masi, A., Kusch, S., Sadori, L., John, S., Francke, A., Wagner, B., & Rethemeyer, J. (2017). Organic geochemical and palynological evidence for Holocene natural and anthropogenic environmental change at Lake Dojran (Macedonia/Greece). *Holocene, 27*(8), 1103–1114. doi:10.1177/0959683616683261

Vinson, G.L. (1962). Upper Cretaceous and Tertiary Stratigraphy of Guatemala. *Bulletin of the American Association of Petroleum Geologists, 46*(4), 425–456.

Volkman, J.K. (2003). Sterols in microorganisms. *Appl. Microbiol. Biotechnol., 60*, 495–506. doi:10.1007/s00253-002-1172-8

Wahl, D., Estrada-Belli, F., & Anderson, L. (2013). A 3400 year paleolimnological record of prehispanic human-environment interactions in the Holmul region of the southern Maya lowlands. *Palaeogeogr. Palaeoclimatol. Palaeoecol., 379-380*, 17–31. doi:10.1016/j.palaeo.2013.03.006

White, A.J., Stevens, L.R., Lorenzi, V., Munoz, S.E., Lipo, C.P., & Schroeder, S. (2018). An evaluation of fecal stanols as indicators of population change at Cahokia, Illinois. *J. Archaeol. Sci., 93*, 129–134. doi:10.1016/j.jas.2018.03.009

Whitlock, C., & Larsen, C. (2001). Charcoal as a fire proxy. In J.P. Smol, H.J.B. Birks, & W.M. Last (Eds.), *Tracking Environmental Change Using Lake Sediments. Volume 3: Terrestrial, Algal, and Siliceous Indicators*, (pp. 75–97). Dordrecht, The Netherlands: Kluwer Academic Publishers.

Wright, D.K., MacEachern, S., Ambrose, S.H., Choi, J., Choi, J.-H., Lang, C., & Wang, H. (2019). Iron Age landscape changes in the Benoué River Valley, Cameroon. *Quat. Res., 92*, 323–339. doi:10.1017/qua.2019.25

Zocatelli, R., Lavrieux, M., Guillemot, T., Chassiot, L., Milbeau, C.L., & Jacob, J. (2017). Fecal biomarker imprints as indicators of past human land uses: Source distinction and preservation potential in archaeological and natural archives. *J. Archaeol. Sci., 81*, 79–89. doi:10.1016/j.jas.2017.03.010

SECTION

2. CONCLUSIONS

We analyzed multiple variables from a 515-cm-long sediment core from the shallow, western arm of Lake Petén Itzá, northern Guatemala to interpret paleoenvironmental changes associated with human settlement of the riparian Maya archaeological site of Nixtun-Ch'ich'. Fluctuations in fecal sterol and stanol concentrations during the late Early Preclassic Period suggest early Maya occupation of the Candelaria Peninsula ca. 1400 BCE, slightly earlier than the earliest pottery sherds indicate human settlement. Increased charcoal abundance beginning ca. 1080 BCE, which coincides with the first appearance of *Zea mays* (corn) pollen in the lake, suggests the use of swidden agricultural techniques by early Maya populations. Deposition of a thin (~0.5 m thick) Maya clay unit in the western arm of the lake corresponds with constructional activities in Nixtun-Ch'ich' during the Middle and Late Preclassic periods. Gradual shifts in organic matter geochemical proxies in this unit during dense Maya occupation suggest that there was a gradual increase in trophic state from ca. 760 to 20 BCE. Whereas massive Maya-induced siltation as a result of land alterations in other Petén lakes may have suppressed lake productivity, paving of the riparian gridded city of Nixtun-Ch'ich' may have enhanced nutrient-laden runoff from the urban center, which fueled primary productivity in the relatively shallow and hydrologically isolated western basin of Lake Petén Itzá. Increased average coprostanol+epicoprostanol concentrations during this time also suggest increased human fecal contamination of the western arm of the lake during the Middle and Late Preclassic. However, upon the reduction or cessation of constructional activities in Nixtun-Ch'ich', the lake experienced a swift, but limited, recovery over ~80 years (from ca. 20 BCE to 60 CE), potentially reflecting partial abandonment of the site during the Terminal Preclassic. Afterward, fecal stanol concentrations suggest relatively low, albeit fluctuating, Maya population densities throughout the Classic and Postclassic Periods. Continued, low-level occupation of Nixtun-Ch'ich' during the Classic and Postclassic may have contributed to the lake's limited recovery.

This study demonstrates that ancient lowland Maya civilization had a substantial impact on the lacustrine environment of Lake Petén Itzá, with eutrophic conditions lasting almost 800 years during dense Maya occupation of Nixtun-Ch'ich'. However, the rapid decline of trophic status over approximately 80 years, upon the abrupt reduction or cessation of substantial constructional activities on the Candelaria Peninsula, shows that lacustrine environments can be resilient when anthropogenic stressors are reduced.

BIBLIOGRAPHY

Adams, R.E.W. (1973). The collapse of Maya civilization: a review of previous theories. In Culbert, T.P. (Ed.), *The Classic Maya Collapse* (pp. 21–34). Albuquerque, New Mexico: Univ. New Mexico Press.

Anselmetti, F.S., Hodell, D.A., Ariztegui, D., Brenner, M., & Rosenmeier, M.F. (2007). Quantification of soil erosion rates related to ancient Maya deforestation. *Geology*, *35*(10), 915–918. doi: 10.1130/G23834A.1

Battistel, D., Roman, M., Marchetti, A., Kehrwald, N.M., Radaelli, M., Balliana, E., Toscano, G., & Barbante, C. (2018). Anthropogenic impact in the Maya Lowlands of Petén, Guatemala, during the last 5500 years. *J. Quat. Sci.*, *33*(2), 166–176. doi: 10.1002/jqs.3013

Beach T., Luzzadder-Beach, S., Cook, D., Dunning, N., Kennett, D.J., Krause, S., Terry, R., Trein, D., & Valdez, F. (2015). Ancient Maya impacts on the Earth's surface: An Early Anthropocene analog? *Quat. Sci. Rev.*, *124*, 1–30. doi:10.1016/j.quascirev.2015.05.028

Beach T., Luzzadder-Beach, S., Krause, S., Guderjan, T., Valdez Jr., F., Fernandez-Diaz, J.C., Eshleman, S., & Doyle, C. (2019). Ancient Maya wetland fields revealed under tropical forest canopy from laser scanning and multiproxy evidence. *Proc. Natl. Acad. Sci. U.S.A.*, *116*(43), 21469–21477. doi:10.1073/pnas.1910553116

Brenner, M., Rosenmeier, M.F., Hodell, D.A., & Curtis, J.H. (2002). Paleolimnology of the Maya Lowlands: Long-term perspectives on interactions among climate, environment, and humans. *Ancient Mesoamerica*, *13*, 141–157. doi:10.1017.S0956536102131063

Chorus, I., Köhler, A., Beulker, C., Fastner, J., van de Weyer, K., Hegewald, T., & Hupfer, M. (2020). Decades needed for ecosystem components to respond to a sharp and drastic phosphorus load reduction. *Hydrobiologia*, *847*, 4621–4651. doi:10.1007/s10750-020-04450-4

Deevey, E.S. (1985). Stress, Strain, and Stability of Lacustrine Ecosystems. In E.Y. Haworth & J.W.G. Lund (Eds.), *Lake Sediments and Environmental History* (pp. 203–229). Minneapolis, MN: University of Minnesota Press.

Deevey, E.S., Rice, D.S., Rice, P.M., Vaughan, H.H., Brenner, M., & Flannery, M.S. (1979). Maya Urbanism: Impact on a Tropical Karst Environment. *Science*, *206*, 298–306.

Douglas, P.M.J., Demarest, A.A., Brenner, M., & Canuto, M.A. (2016). Impacts of Climate Change on the Collapse of Lowland Maya Civilization. *Annu. Rev. Earth Planet. Sci., 44*, 613–645. doi:10.1146/annurev-earth-060115-012512

Douglas, P.M.J., Pagani, M., Canuto, M.A., Brenner, M., Hodell, D.A., Eglinton, T.I., & Curtis, J.H. (2015). Drought, agricultural adaptation, and sociopolitical collapse in the Maya Lowlands. *Proc. Natl. Acad. Sci. U.S.A., 112*(18), 5607–5612. doi:10.1073/pnas.1419133112

Dunning, N.P., Beach, T.P., & Luzzadder-Beach, S. (2012). Kax and kol: Collapse and resilience in lowland Maya civilization. *Proc. Natl. Acad. Sci. U.S.A., 109*(10), 3652–3657. doi:10.1073/pnas.1114838109

Gallant, L.R., Kimpe, L.E., Hargan, K.E., & Blais, J.M. (2020). Tracking the history of 20th century cultural eutrophication in High Arctic waterbodies. *Anthropocene, 31*, 100250. doi:10.1016/j.ancene.2020.100250

Hodell, D.A., Curtis, J.H., & Brenner, M. (1995). Possible role of climate in the collapse of Classic Maya civilization. *Nature, 375*, 391–394.

Jilbert, T., Couture, R-M., Huser, B.J., & Salonen, K. (2020). Preface: Restoration of eutrophic lakes: current practices and future challenges. *Hydrobiologia, 847*, 4343–4357. Doi:10.1007/s10750-020-04457-x

Krause, S., Beach, T.P., Luzzadder-Beach, S., Cook, D., Bozarth, S.R., Valdez Jr., F., & Guderjan, T.H. (2021). Tropical wetland persistence through the Anthropocene: Multiproxy reconstruction of environmental change in a Maya agroecosystem. *Anthropocene, 34*, 100284. doi:10.1016/j.ancene.2021.100284

Li, C., Feng, W., Song, F., He, Z., Wu, F., Zhu, Y., Giesy, J.P., & Bai, Y. (2019). Three decades of changes in water environment of a large freshwater Lake and its relationship with socio-economic indicators. *Journal of Environmental Sciences, 77*, 156–166. doi:10.1016/j.jes.2018.07.001

Mueller A.D., Islebe, G.A., Hillesheim, M.B., Grzesik, D.A., Anselmetti, F.S., Ariztegui, D., Brenner, M., Curtis, J.H., Hodell, D.A., & Venz, K.A. (2009). Climate drying and associated forest decline in the lowlands of northern Guatemala during the late Holocene. *Quat. Res., 71*, 133–141. doi:10.1016/j.yqres.2008.10.002

Pugh, T.W., Rice, P.M., Chan Nieto, E.M., Meranda, M.L., & Milley, D.S. (in press). Middle Preclassic hydraulic planning at Nixtun-Ch'ich', Petén, Guatemala. *Ancient Mesoamerica*.

Rice, P.M., & Pugh, T.W. (2021). Middle Preclassic Nixtun-Ch'ich': A lowland Maya primate/ritual city. *J. Anthropol. Archaeol., 63*, 101308. doi:10.1016/j.jaa.2021.101308

Singh, G., & Patidar, S.K. (2020). Water quality restoration by harvesting mixed culture microalgae using *Moringa oleifera*. *Water Environ. Res., 92*, 1268–1282. doi:10.1002/wer.1322

Turner II, B.L., & Sabloff, J.A. (2012). Classic Period collapse of the Central Maya Lowlands: Insights about human-environment relationships for sustainability. *Proc. Natl. Acad. Sci. U.S.A., 109*(35). 13908–13914. doi:10.1073/pnas.1210106109

Vinson, G.L. (1962). Upper Cretaceous and Tertiary Stratigraphy of Guatemala. *Bulletin of the American Association of Petroleum Geologists, 46*(4), 425–456.

Wahl, D., Estrada-Belli, F., & Anderson, L. (2013). A 3400 year paleolimnological record of prehispanic human-environment interactions in the Holmul region of the southern Maya lowlands. *Palaeogeogr. Palaeoclimatol. Palaeoecol., 379–380,* 17–31. doi:10.1016/j.palaeo.2013.03.006

VITA

Brooke Amber Birkett was born in Missouri. In July 2020, she graduated summa cum laude with a Bachelor of Science in Geology and Geophysics and minors in Geological Engineering, Spanish, and Latin American Studies for Technical Applications from Missouri University of Science and Technology, Rolla, Missouri, USA. While at Missouri S&T, she was a Curator's Scholar and a National Action Council for Minorities in Engineering (NACME) Scholar. She also received the Ray E. Morgan Award for Special Achievement in Geology in 2019 and the Dr. Robert Laudon Advanced Field Camp Award in 2020 during her undergraduate studies. During her graduate career, she earned the Dr. Alfred Spreng Graduate Research Award in 2020. She received her Master of Science in Geology and Geophysics from Missouri University of Science and Technology, Rolla, Missouri, USA in December 2021.